Inertial wave activity during spin-down in a rapidly rotating penny shaped cylinder

Ludivine Oruba, A.M. Soward, E. Dormy

Inertial wave activity during spin-down in a rapidly rotating penny shaped cylinder

L. Oruba[1],† A. M. Soward[2],†, and E. Dormy[3],†

[1]Laboratoire Atmosphères Milieux Observations Spatiales (LATMOS/IPSL), Sorbonne Université, UVSQ, CNRS, Paris, FRANCE

[2]School of Mathematics and Statistics, Newcastle University, Newcastle upon Tyne NE1 7RU, UK

[3]Département de Mathématiques et Applications, UMR-8553, École Normale Supérieure, CNRS, PSL University, 75005 Paris, FRANCE

(Received xx; revised xx; accepted xx)

In an earlier paper, Oruba, Soward & Dormy (J. Fluid Mech., vol. 818, 2017, pp. 205–240) considered the primary quasi-steady geostrophic (QG) motion of a constant density fluid of viscosity ν that occurs during linear spin-down in a cylindrical container of radius L and height H, rotating rapidly (angular velocity Ω) about its axis of symmetry subject to mixed rigid and stress-free boundary conditions for the case $L = H$. Direct Numerical Simulation (DNS) at large $L = 10H$ and Ekman number $E \leqslant \nu/H^2\Omega = 10^{-3}$ by Oruba, Soward & Dormy (J. Fluid Mech., vol. 888, A9, 2020, pp. 44) reveals significant inertial wave activity on the spin-down time-scale. That analytic study, for $E \ll 1$, builds on the results of Greenspan & Howard (J. Fluid Mech., vol. 17, 1963, pp. 385–404) for an infinite plane layer $L \to \infty$. At large but finite distance $r^\dagger$ from the symmetry axis, the meridional (QG-)flow, that causes the QG-spin down, is blocked by the lateral boundary $r^\dagger = L$, which provides the primary QG-trigger for inertial wave generation. For the laterally unbounded layer, Greenspan & Howard identified, in addition to the QG-flow, inertial waves of maximum frequency (MF) 2Ω, which are a manifestation of the transient Ekman layer, decaying algebraically in time. The blocking of these additional MF-waves by the lateral boundary (ignored by Oruba *et al.* 2020) provides an additional trigger that complements the QG-triggered inertial waves. Here we obtain analytic results for the full wave activity caused by the combined-trigger (QG+MF) that faithfully capture the character of the laterally bounded base flow including its transients. The results are compared with the inertial wave part of the DNS (the so called 'filtered DNS' or simply 'FNS'), for which the agreement is excellent and accounts for minor discrepancies evident in the previous QG-trigger results.

1. Introduction

Our study is motivated by the understanding of large scale nearly axisymmetric vortices in the atmosphere, such as tropical cyclones, also referred to as hurricanes or typhoons. Oscillations have been observed near the eye of actual tropical cyclones (e.g., Harlow & Stein 1974; Chen *et al.* 2015). These are reminiscent of inertial waves and exhibit similar periods (Atkinson *et al.* 2019). A clean cut mathematical model is needed in order to investigate these waves. We therefore investigate inertial wave activity in a penny shaped cylinder in solid body rotation for which the angular velocity of the container is abruptly changed.

† Email address for correspondence: ludivine.oruba@latmos.ipsl.fr, andrew.soward@ncl.ac.uk, Emmanuel.Dormy@ens.fr

In Oruba *et al.* (2020), we investigated the inertial wave response during spin-down in a shallow cylinder height H, of large radius $L\,(\gg H)$ equivalently

$$\ell \,\equiv\, L/H \gg 1\,, \tag{1.1}$$

by consideration of a "reduced model". Here we consider the complete problem. On the one hand, we refrain from repeating some of the references cited in Oruba *et al.* (2020), which apply equally here. On the other, as we need to refer extensively to equations (say $(x.y)$), sections (say §x) and figures (say figure x) from Oruba *et al.* (2020) (say $\mathcal{O}$), we use the notation "($\mathcal{O}$: $x.y$)", "§$\mathcal{O}$:x" and "figure $\mathcal{O}$:x" respectively to identify them.

Our cylindrical container is filled with constant density fluid of viscosity ν and rotates rigidly with angular velocity $\boldsymbol{\varOmega}$ about its axis of symmetry, the frame, relative to which our analysis is undertaken; the Ekman number is small:

$$E \,=\, \nu\big/\big(H^2\varOmega\big) \,\ll\, 1\,. \tag{1.2}$$

Initially, at time $t^\dagger = 0$, the fluid itself rotates rigidly at the slightly larger angular velocity $Ro\,\boldsymbol{\varOmega}$, in which the Rossby number Ro is sufficiently small ($Ro \ll E^{1/4}$) for linear theory to apply. Relative to cylindrical polar coordinates, ($r^\dagger$, $\theta^\dagger$, $z^\dagger$), the top boundary ($r^\dagger < L$, $z^\dagger = H$) and the side-wall ($r^\dagger = L$, $0 < z^\dagger < H$) are impermeable and stress-free. The bottom boundary ($r^\dagger < L$, $z^\dagger = 0$) is rigid. For that reason alone the initial state of relative rigid rotation $Ro\,\boldsymbol{\varOmega}$ of the fluid cannot persist and the fluid spins down to the final state of no rotation relative to the container, as $t^\dagger \to \infty$. We describe the transient relative motion, velocity $\boldsymbol{v}^\dagger$, by its cylindrical components oriented by the rotation axis, which we partition into its horizontal $\boldsymbol{v}_\perp^\dagger = [u^\dagger, v^\dagger]$ and vertical $w^\dagger$ components.

Whereas an actual tropical cyclone is in essence living in an unbounded flow (at the surface of a sphere), models of axisymmetric geophysical vortices in general (e.g., Williams 1968; Read 1986a,b; Rotunno 1979, 2014) and of tropical cyclones in particular (e.g., Rotunno & Emanuel 1987; Montgomery *et al.* 2001) are in essence bounded. The same would be true of any experimental setup. In the particular setup investigated here, inertial wave activity is triggered by the outer bounding wall. In a true cyclone, they will be triggered by other disturbances (such as non-axisymmetric heterogeneities) but will be equally important. In practice, they may also interact nonlinearly (e.g., Yarom & Sharon 2014). Here we restrict our attention to the exact linear ($Ro \ll 1$) solution for a bounded flow, relevant to either a numerical model or laboratory experiment, both bounded. We describe mathematically how the waves triggered at the outer boundary propagate toward the axis and reasonably expect that some of the qualitative wave behaviour predicted will not simply depend on our chosen forcing but apply equally to real tropical cyclones. Indeed, we believe that our waves can shed light on understanding the inertial wave activity observed near the axis of cyclones (e.g., Chen *et al.* 2015).

Inertial waves in confined flows, driven by the relative motion of boundaries, is of continued topical interest, from both experimental and theoretical points of view (see Klein *et al.* 2014; Kurgansky *et al.* 2020, and references therein). The special case of linear spin-down, manifest primarily by a Quasi-Geostrophic (QG) flow (largely time dependent rigid rotation) caused by axial vortex line shortening due to blowing from the Ekman layers, is well understood (see, e.g., Benton & Clark 1974; Duck & Foster 2001). However, the secondary generation of inertial waves during spin-down has received less attention. Though, in the case of a cylinder, their wave spectrum and viscous decay rates are well understood (see, e.g., Kerswell & Barenghi 1995; Zhang & Liao 2008, and references therein), we are only aware of one study (Cederlöf 1988) that addresses the issue of wave amplitude analytically.

Our development builds on a laterally unbounded model ($L \to \infty$) studied in considerable detail by Greenspan & Howard (1963), for which a useful summary and clarifying description are given in sections 2.3 and 2.4 of Greenspan (1968). We emphasise, at the outset, that mathematically our use of a stress-free boundary at $z^\dagger = H$ is equivalent to theirs on doubling our gap height and applying no-slip boundary conditions at $z^\dagger = 2H$ instead. The equivalence follows from symmetries, $z^\dagger \mapsto 2H - z^\dagger$, about the mid-plane $z^\dagger = H$. Greenspan & Howard (1963) also considered the role of the outer rigid boundary at $r^\dagger = L$ and particularly the boundary layer structure there.

The spin-down process operates on three time-scales identified by

$$\Omega t^\dagger = \begin{cases} O(1)\,, & \text{Rotation or inertial wave time,} \\ O(E^{-1/2})\,, & \text{Spin-down time,} \\ O(E^{-1})\,, & \text{Transverse diffusion time.} \end{cases}$$

We will refer to these regimes repeatedly.

Oruba *et al.* (2017) pointed out that a QG-layer, close to the outer $r^\dagger = L$ boundary, spreads inwards towards the $r^\dagger = 0$ axis broadening indefinitely. Curiously, when that outer boundary is stress-free, the returning meridional flow is not impeded by boundary friction. So, to a small extent, rather than promoting spin-down by compressing axial vortex lines, the opposite tends to happen. The consequence of this weak tendency is to slightly slow spin-down on the long transverse diffusion time-scale $\Omega t^\dagger = O(E^{-1})$. Here and in our previous work Oruba *et al.* (2020), we are not concerned with that QG-development, but rather focus attention on the evolution of inertial waves triggered simply by the impermeable boundary condition $u^\dagger = 0$ at $r^\dagger = L$ on the shorter time-scales $\Omega t^\dagger \ll E^{-1}$. For that, whether the lateral boundary $r^\dagger = L$ is no-slip or stress-free is irrelevant and has no influence on the inertial wave activity "triggered" by the blocking of the radial flow found in the unbounded domain $L \to \infty$. Fortunately, to compare our inertial wave predictions with the results of Direct Numerical Simulation (DNS) based on the entire governing equations, we are able to filter out the mainstream QG-contribution (as well as the inertial wave contribution, with frequency close to 2, in the trigger flow identified by Greenspan 1968) to expose only the triggered inertial waves. The filtered waves are the same whether the outer boundary $r^\dagger = L$ is no-slip or stress-free.

In short, our approach builds on the idea that the radial outflow for the unbounded case is simply blocked, $u^\dagger = 0$ at $r^\dagger = L$ with, at leading order, the stress boundary condition only affecting the QG-flow contribution studied by Oruba *et al.* (2017). Our asymptotic analysis only applies when $\Omega t^\dagger \ll E^{-1}$. Oruba *et al.* (2020) ignored the early time $\Omega t^\dagger = O(1)$ behaviour. Though, this is adequate to capture the main features of the triggered wave solution, it is not asymptotically correct. For surprisingly the $\Omega t^\dagger = O(1)$ behaviour of the unbounded flow has a persistent influence on the solution. Its most evident consequences are a phase lag and smaller amplitude of the Oruba *et al.* (2020) triggered waves relative to the asymptotically correct wave solution derived here.

In order to make our notation relatively compact at an early stage, we use H and Ω^{-1} as our unit of length and time respectively, and introduce

$$r^\dagger = Hr\,, \qquad z^\dagger = Hz\,, \qquad \Omega t^\dagger = t\,, \qquad \boldsymbol{v}^\dagger = Ro\,L\Omega\,\boldsymbol{v}\,, \tag{1.3a–d}$$

in which for our unit of relative velocity $\boldsymbol{v}^\dagger$, we have adopted the velocity increment $Ro\,L\Omega$ of the initial flow at the outer boundary $r^\dagger = L$. The cylindrical component axisymmetric velocity decomposition becomes

$$\boldsymbol{v}(r,z,t) = [\boldsymbol{v}_\perp,\, w] \qquad \text{with} \qquad \boldsymbol{v}_\perp = [u,\, v] \tag{1.4a,b}$$

and, on introduction of the meridional flow streamfunction $r\chi$, we have

$$u \,=\, -\,\frac{\partial \chi}{\partial z}\,, \qquad\qquad w \,=\, \frac{1}{r}\frac{\partial (r\chi)}{\partial r}\,. \tag{1.4c,d}$$

In this Introduction, we summarise and expand on the results of Greenspan & Howard (1963), as needed to properly understand the nature of the unbounded, $\ell = L/H \to \infty$, spin-down flow which provides the inertial wave trigger in the bounded case at $r = \ell$. Like Greenspan & Howard (1963), our development relies heavily on the Laplace transform (LT), an operation $\mathcal{L}$ leading to values denoted by the $\widehat{\ }$ accent, e.g.,

$$\widehat{\boldsymbol{v}}(r,z,p) \,=\, \mathcal{L}\{\boldsymbol{v}\} \,\equiv\, \int_0^\infty \boldsymbol{v}(r,z,t)\, \exp(-pt)\, \mathrm{d}t \tag{1.5a}$$

with inverse-LT

$$\boldsymbol{v}(r,z,t) \,=\, \mathcal{L}^{-1}\{\widehat{\boldsymbol{v}}\} \,\equiv\, \frac{1}{2\pi\mathrm{i}}\int_{-\mathrm{i}\infty}^{\mathrm{i}\infty} \widehat{\boldsymbol{v}}(r,z,p)\exp(pt)\, \mathrm{d}p\,. \tag{1.5b}$$

The complete LT-solution of the $\ell \to \infty$ problem is given by equations (3.4), (3.5) of Greenspan & Howard (1963). Crucially, the LTs involve cut-points at $p = \pm 2\mathrm{i}$, exemplified by the factors $(p \mp 2\mathrm{i})^{1/2}$ which appear in their equations (3.6). The cut-points are illusory and not part of the solution, which only possesses poles. In the small Ekman number limit $E \ll 1$, a pole near $p = 0$ identifies the QG-spin-down mode, while an infinite sequence of densely packed poles to the left of the "illusory" cuts at $p = \pm 2\mathrm{i}$ identifies modes with distinct viscous decay rates with frequencies close to 2 (see Greenspan & Howard 1963, equations (3.7), (3.8)). The later pole-family is needed to properly resolve late time behaviour, $t = O(E^{-1})$. At shorter times $t < O(E^{-1})$ a different tactic for the LT-inversion (see Greenspan & Howard 1963, p. 389, 390), which essentially reinstates the "illusory" cuts, is more useful. That strategy can only be undertaken with considerable caution, as the asymptotic approach has limitations that must be clearly understood. To that end, we build the picture slowly through the survey §§1.1, 1.2 (essentially a considerable expansion of Greenspan 1968, sections 2.3 and 2.4, respectively, with an alternative perspective) of a hierarchy of problems that highlight the main ideas. Then, in §1.3, we identify (1.29) as an approximation to the inertial wave trigger, sufficiently accurate for our purposes over the entire time $0 < t \ll E^{-1}$. We outline the organisation of our paper in §1.4.

1.1. *The transient Ekman layer*

The transient Ekman layer, in the half-space $z > 0$ above a rigid boundary $z = 0$, is well known (see, e.g., Greenspan 1968, section 2.3). Still, we provide here a summary in order to develop our notation and highlight features upon which we will build. Significantly, as the LT-solution ((1.11) below) involves both a pole at $p = 0$ and cuts at $p = \pm 2\mathrm{i}$, we may immediately identify the seeds of spin-down and inertial wave generation between parallel planes. For that, the cuts are strictly removed by the inclusion of an upper boundary, as previously mentioned.

We consider the axisymmetric flow in the self-similar form

$$\boldsymbol{v}_\perp \,=\, (r/\ell)\,[\mathfrak{u}(z,t)\,,\, \mathfrak{v}(z,t)]\,, \qquad\qquad w \,=\, (1/\ell)\,\mathfrak{w}(z,t)\,, \tag{1.6a,b}$$

that solves

$$\partial_t \mathfrak{u} \,-\, 2\,(\mathfrak{v}-1) \,=\, E\partial_z^2 \mathfrak{u}\,, \qquad\qquad \partial_t \mathfrak{v} \,+\, 2\,\mathfrak{u} \,=\, E\partial_z^2 \mathfrak{v} \tag{1.7a,b}$$

subject to $[\,\mathfrak{u}\,,\,\mathfrak{v}\,] = [0,\,1]$ at $t = 0$, while subsequently $[\,\mathfrak{u}\,,\,\mathfrak{v}\,] = [0,\,0]$ at $z = 0$ and

$[\mathfrak{u}\,,\,\mathfrak{v}\,] \to [0,\,1]$ as $z \uparrow \infty$ for $t > 0$. Of interest to us is the horizontal boundary layer volume flux deficit

$$-\,E^{1/2}\,\frac{r}{\ell}\,\big[\,\mathfrak{U}(t)\,,\,\mathfrak{V}(t)\big] \;=\; \frac{r}{\ell}\int_0^\infty [\,\mathfrak{u}\,,\,\mathfrak{v}-1\,]\,\mathrm{d}z\,. \tag{1.8}$$

By mass continuity, the outflow velocity $E^{1/2}\,\mathfrak{W}/\ell$ from it is determined from

$$\mathfrak{W}(t) \;\equiv\; E^{-1/2}\mathfrak{w}_{z\uparrow\infty} \;=\; 2\mathfrak{U}(t)\,. \tag{1.9}$$

The minus sign in (1.8) is motivated by our application to spin-down between two unbounded parallel plates, $0<z<1$, in the next §1.2.

In terms of the complex combinations

$$\mathfrak{z}^{\pm}(z,t) \;=\; \mathfrak{u} \pm \mathrm{i}\big(\mathfrak{v}-1\big)\,, \qquad\qquad \mathfrak{W}^{\pm}(t) \;=\; \mathfrak{U} \pm \mathrm{i}\mathfrak{V}\,, \tag{1.10a,b}$$

the LT-solutions are

$$\widehat{\mathfrak{z}}^{\pm}(z,p) \;=\; \mp\,\mathrm{i}p^{-1}\exp\!\big[-E^{-1/2}(p\pm 2\mathrm{i})^{1/2}z\big]\,, \tag{1.11a}$$

$$\widehat{\mathfrak{W}}^{\pm}(p) \;=\; \pm\,\mathrm{i}p^{-1}(p\pm 2\mathrm{i})^{-1/2}\,. \tag{1.11b}$$

The inverse-LT of the former is discussed in appendix A, while the latter is

$$\mathfrak{W}^{\pm}(t) \;=\; \tfrac{1}{2}(1\pm\mathrm{i})\,\mathrm{erf}\,\big[(1\pm\mathrm{i})t^{1/2}\big]\,, \tag{1.12a}$$

which, by ((http://dlmf.nist.gov/7.5.E8) of Abramowitz & Stegun 2010) has the alternative representation

$$=\mathrm{S}(T)\;\pm\;\mathrm{i}\,\mathrm{C}(T)\,, \qquad\qquad T(t) \;=\; \sqrt{4t/\pi}\,, \tag{1.12b}$$

in terms of the Fresnel integrals C and S (http://dlmf.nist.gov/7.2.E7,8). Hence (1.9) and (1.10b) determine

$$\mathfrak{W}(t) \;=\; 2\mathfrak{U}(t) \;=\; \mathfrak{W}^{+}(t) \;+\; \mathfrak{W}^{-}(t)\,, \tag{1.12c}$$

$$\begin{bmatrix}\mathfrak{U}(t)\\ \mathfrak{V}(t)\end{bmatrix} \;=\; \begin{bmatrix}\mathrm{S}(T)\\ \mathrm{C}(T)\end{bmatrix} \;=\; \int_0^t \begin{bmatrix}\sin(2\tau)\\ \cos(2\tau)\end{bmatrix}\frac{\mathrm{d}\tau}{\sqrt{\pi\tau}}\,. \tag{1.12d}$$

As $\mathfrak{W}^{-}(t)$ is the complex conjugate of $\mathfrak{W}^{+}(t)$, the $\pm$-notation is unnecessary at this stage. In the spirit of our notation development, however, we introduce it here anticipating the later generalisation in §2.2 to $\mathfrak{W}^{\mathsf{d}\pm}_{mn}(t)$ with LT (2.19d), which is needed to describe the wave response in our closed cylinder to excitation at a frequency ω_{mn}.

For $t = O(1)$, the inverse-LT of (1.11a) describes a complicated boundary layer structure of width

$$\varDelta(t) \;=\; \sqrt{Et}\,, \tag{1.13}$$

just as for all evolving viscous layers.

For $t \gg 1$, the boundary layer splits into two parts:

(i) *Steady.* The final steady Ekman layer, width $\varDelta_{E} = \varDelta(1) = \sqrt{E}$, generated by the pole $p = 0$ of (1.11) has

$$\mathfrak{z}^{\pm}_{E}(z) \;=\; \lim_{t\to\infty}\mathfrak{z}^{\pm}(z,t) \;=\; \mp\mathrm{i}\exp[-(1\pm\mathrm{i})z/E^{1/2}]\,, \tag{1.14a}$$

$$\mathfrak{W}^{\pm}_{E} \;=\; \lim_{t\to\infty}\mathfrak{W}^{\pm}(t) \;=\; \tfrac{1}{2}(1\pm\mathrm{i})\,, \tag{1.14b}$$

leading to the corresponding $\mathfrak{u}$, $\mathfrak{v}$, $\mathfrak{U}$, $\mathfrak{V}$, $\mathfrak{W}$ values

$$[\mathfrak{u}_{E}(z)\,,\,\mathfrak{v}_{E}(z)-1] \;=\; -\;\exp(-z/E^{1/2})\big[\sin(z/E^{1/2})\,,\,\cos(z/E^{1/2})\big]\,, \tag{1.15a}$$

$$\mathfrak{U}_{E} \;=\; \mathfrak{V}_{E} \;=\; \tfrac{1}{2}\,, \qquad\qquad \mathfrak{W}_{E} \;=\; 2\mathfrak{U}_{E} \;=\; 1\,. \tag{1.15b}$$

(ii *a*) *Transient,* $\forall t$. The remaining transient layer may be described by the forms

$$\mathfrak{z}^{\pm}_{MF}(z,t) \,=\, \mathfrak{z}^{\pm}(z,t) \,-\, \mathfrak{z}^{\pm}_{E}(z) \,=\, \mathfrak{h}^{\pm}_{MF}(z,t)\exp\left[-\frac{z^2}{4Et} \mp 2\mathrm{i}t\right], \tag{1.16a}$$

$$\mathfrak{W}^{\pm}_{MF}(t) \,=\, \mathfrak{W}^{\pm}(t) \,-\, \mathfrak{W}^{\pm}_{E}(t) \,=\, -\,\tfrac{1}{2}(1\pm\mathrm{i})\,\mathrm{erfc}\left[(1\pm\mathrm{i})t^{1/2}\right] \tag{1.16b}$$

$$= \,-\,\left[f(T) \pm \mathrm{i}g(T)\right]\exp(\mp 2\mathrm{i}t)\,, \tag{1.16c}$$

the details of which we now explain. The relationship between (1.16*b*,*c*) follows from (http://dlmf.nist.gov/7.5.E10), where the auxiliary functions *f*, *g* are defined in §http://dlmf.nist.gov/7.2.iv. Equations (1.12) and (1.16*b*,*c*) determine

$$\begin{bmatrix}\mathfrak{U}_{MF}(t)\\ \mathfrak{V}_{MF}(t)\end{bmatrix} \,=\, -\int_t^{\infty}\begin{bmatrix}\sin(2\tau)\\ \cos(2\tau)\end{bmatrix}\frac{\mathrm{d}\tau}{\sqrt{\pi\tau}} \,=\, -\begin{bmatrix}f(T)\cos(2t)+g(T)\sin(2t)\\ -f(T)\sin(2t)+g(T)\cos(2t)\end{bmatrix}, \tag{1.17a}$$

$$\mathfrak{W}_{MF}(t) \,=\, 2\mathfrak{U}_{MF}(t)\,. \tag{1.17b}$$

The function $\mathfrak{h}^{\pm}_{MF}$ in (1.16*a*) is defined by (A 3) in appendix A, also in terms of f and g.

(ii *b*) *Transient,* $t \gg 1$. We emphasise that for $t \leqslant O(1)$, the E/MF-partition (1.14)–(1.17) is unhelpful and, though correct, the features suggested by (1.16*a*,*c*) are misleading at that early time. However, when $t \gg 1$, their defining functions *f*, *g* have algebraic asymptotic expansions (http://dlmf.nist.gov/7.12.E2, E3). Then, the exponent $\exp(-z^2/4Et)$ in (1.16*a*) clearly identifies the boundary layer width $\mathit{\Delta}(t)$, as it does in the asymptotic form (A 7) for the boundary layer flow $[\mathfrak{u}_{MF}(z,t),\, \mathfrak{v}_{MF}(z,t)]$ derived in appendix A. Likewise, the exponent $\exp(\mp 2\mathrm{i}t)$ in (1.16*a*,*c*) identifies inertial waves of Maximum Frequency 2. In reality they are modulated and so we refer to such quasi-waves as MF-waves; whence our use of the subscript 'MF'.

1.2. *Spin-down between two unbounded parallel plates*

In our small E-limit, the spin-down between two unbounded parallel plates $z = 0,\, 1$ may be decomposed into its mainstream $\overline{\boldsymbol{v}}$ and boundary layer $\boldsymbol{v}^{\vartriangle}$ parts. The horizontal contribution $\overline{\boldsymbol{v}}_{\perp}$ is z-independent, while $\boldsymbol{v}^{\vartriangle}_{\perp}$ is of the E/MF-layer type described in §1.1. However, whereas the vertically unbounded mainstream flow $\overline{\boldsymbol{v}}$ described there was simply $[0,\, r,\, E^{1/2}\mathfrak{W}(t)]/\ell$, when the upper boundary $z = 1$ is included, the uniform axial outflow $(E^{1/2}/\ell)\mathfrak{W}(t)$ from the boundary layer is blocked and obliged to escape radially instead, causing quasi-geostrophic (QG) spin-down. As in §1.1, we find it convenient to partition the flows into their (i) E- (or rather QG-) and (ii) MF-constituents $\boldsymbol{v}_{QG}$ and $\boldsymbol{v}_{MF}$ respectively. To understand the nature of the motion, in the following §1.2.1, we consider $\overline{\boldsymbol{v}}_{MF\perp}$ on the transient Ekman layer time scale $t = O(1)$, during which $\overline{\boldsymbol{v}}_{QG\perp} \approx [0,\, r/\ell]$ as in §1.1. Then in §1.2.2, we explain the modifications appropriate on the longer spin-down time $t = O(E^{-1/2})$ over which the QG-flow $\overline{\boldsymbol{v}}_{QG\perp}$ evolves. That analysis is restricted to $t \ll E^{-1}$ by the requirement that the MF boundary layer width $\mathit{\Delta}(t) = \sqrt{Et}$ be small compared to the plate separation unity.

Throughout this section we continue to employ the similarity representation (1.6*a*) with Fraktur variables, $\overline{\boldsymbol{v}}_{\perp} = (r/\ell)[\overline{\mathfrak{u}}(t),\, \overline{\mathfrak{v}}(t)]$, and use the aforesaid notations $\overline{\bullet}$ and $\bullet^{\vartriangle}$ to identify respectively mainstream and boundary layer parts.

1.2.1. *The transient Ekman layer time* $t = O(1)$

For $t \ll E^{-1/2}$, short compared to the spin-down time, we regard any modification to the initial value $[\,\overline{\mathfrak{u}},\, \overline{\mathfrak{v}}\,] = [0,\, 1]$ as a perturbation. On that basis we may employ but suitably modify the results of §1.1.

To begin, the ejected volume flux, $E^{1/2}\,\mathfrak{W}/\ell = 2E^{1/2}\,\mathfrak{U}/\ell$ (see (1.9)) from the Ekman layer, drives the mainstream radial flow $\overline{u} = (r/\ell)\overline{\mathfrak{u}}$, which by continuity of total radial mass flux is determined by

$$\overline{\mathfrak{u}}(t) \;=\; -\int_0^\infty \mathfrak{u}^\Delta \,\mathrm{d}z \;=\; E^{1/2}\mathfrak{U} \;=\; E^{1/2}\big(\tfrac{1}{2} + \mathfrak{U}_{MF}\big)\,. \tag{1.18a}$$

From (1.4*c*,*d*) the corresponding streamfunction $r\overline{\chi}$ and vertical velocity $\overline{w}$ for the resulting meridional mainstream flow are

$$\overline{\chi} \;=\; (r/\ell)(1-z)\overline{\mathfrak{u}}(t)\,, \qquad\qquad \overline{w} \;=\; (2/\ell)(1-z)\overline{\mathfrak{u}}(t)\,. \tag{1.18b,c}$$

On introduction of z-average,

$$\langle\bullet\rangle \;=\; \textstyle\int_0^1 \bullet \;\mathrm{d}z\,, \tag{1.19}$$

an alternative interpretation of (1.18*a*) is that of vanishing total radial MF mass flux

$$(\ell/r)\langle u_{MF}\rangle \approx \overline{\mathfrak{u}}_{MF} \;-\; E^{1/2}\mathfrak{U}_{MF} \;=\; 0\,. \tag{1.20}$$

On omitting the viscous term in the azimuthal equation of motion (1.7*b*) to obtain $\partial\overline{\mathfrak{v}}/\partial t = -2\overline{\mathfrak{u}}$, integration subject to $\overline{\mathfrak{v}}(0) = 1$ determines

$$\overline{\mathfrak{v}}(t) - 1 \;=\; -\;2\int_0^t \overline{\mathfrak{u}}(\tau)\,\mathrm{d}\tau \;\approx\; -\,2E^{1/2}\int_0^t \mathfrak{U}(\tau)\,\mathrm{d}\tau \tag{1.21a}$$

$$\;=\; -\;E^{1/2}t \;-\; 2E^{1/2}\int_0^t \mathfrak{U}_{MF}(\tau)\,\mathrm{d}\tau\,, \tag{1.21b}$$

on use of (1.18*a*). The natural partition $\overline{\mathfrak{v}} = \overline{\mathfrak{v}}_{QG} + \overline{\mathfrak{v}}_{MF}$ is

$$\overline{\mathfrak{v}}_{QG}(t) \;\approx\; \kappa \;-\; E^{1/2}t\,, \qquad\qquad \overline{\mathfrak{v}}_{MF}(t) \;\approx\; 2E^{1/2}\int_t^\infty \mathfrak{U}_{MF}(\tau)\,\mathrm{d}\tau\,, \tag{1.22a,b}$$

where κ is a constant of integration and the upper integration limit is chosen such that $\overline{\mathfrak{v}}_{MF} \to 0$ as $t \to \infty$. Evaluation of the integral is relegated to appendix B, in which (B 1) determines $\overline{\mathfrak{v}}_{MF}(0) = \frac{1}{2}E^{1/2}\mathfrak{V}_{MF}(0) = -\frac{1}{4}E^{1/2}$, in turn, fixing

$$\kappa \;=\; 1 \;-\; \overline{\mathfrak{v}}_{MF}(0) \;=\; 1 \;+\; \tfrac{1}{4}E^{1/2} \;+\; O(E)\,. \tag{1.22c}$$

The z-average of the pole-residue formula (Greenspan & Howard 1963, second line of equation (3.10)) suggests that a result $(\ell/r)\langle v_{MF}\rangle$ $(\approx \overline{\mathfrak{v}}_{MF} - E^{1/2}\mathfrak{V}_{MF}) \approx 0$, similar to (1.20), holds for the azimuthal flow. Though true asymptotically for $t \gg 1$ (see (1.24) below), (B 2*a*) shows that

$$(\ell/r)\langle v_{MF}\rangle \;\approx\; \overline{\mathfrak{v}}_{MF} - E^{1/2}\mathfrak{V}_{MF} \;=\; E^{1/2}\mathfrak{R}_{MF} \neq 0\,. \tag{1.23}$$

Asymptotic evaluation of the "remainder" $\mathfrak{R}_{MF}$ (see (B 1*b*) and (B 2*b*)) provides the estimates

$$\langle v_{MF}\rangle \;=\; \begin{cases} O(\overline{v}_{MF}) & \text{for} \quad t = O(1)\,, \\ O(t^{-1}\overline{v}_{MF}) & \text{for} \quad t \gg 1\,. \end{cases} \tag{1.24}$$

For us, this has the important implication that, whenever $t \gg 1$, the z-average $\langle v_{MF}\rangle$ is indeed small. This property, together with $\langle u_{MF}\rangle = 0$ (1.20), is needed to justify the DNS-filter described in §5.1 and employed in §5.2; aliter, the filter is only valid for $t \gg 1$.

1.2.2. *The spin-down time $t = O(E^{-1/2})$*

The QG-approximations of the above §1.2.1 are based on the initial assumption that $[\overline{\mathfrak{u}}_{QG}, \overline{\mathfrak{v}}_{QG}]$ remains close to $[0, 1]$. The secular behaviour $E^{1/2}t$ of $\overline{\mathfrak{v}}_{QG}$ in (1.22*a*) explicitly shows that the assumption fails when $E^{1/2}t = O(1)$. As previously mentioned below

(1.5), the complete LT-solution is given by equations (3.4), (3.5) of Greenspan & Howard (1963). That provides the conventional normal mode response (identified by the LT-poles) in a confined geometry, albeit here only by the two boundaries $z = 0$ and 1. The normal modes lead to infinite sums (approximated by Greenspan & Howard 1963, equations (3.9), (3.10)). When those sums are dominated by large harmonics, it is often possible (as shown by Oruba *et al.* 2020, in the MF boundary layer context) to approximate such sums ($\mathcal{O}$: 1.13) by integrals ($\mathcal{O}$: 1.15). This example illustrates the fact that the asymptotic continuum approximation $\sum \mapsto \int$ possesses an inherent error, here $O(E^{1/2})$. For $t \geqslant O(1)$ (following Greenspan & Howard 1963), we adopt that continuum strategy, bearing in mind that we can never improve on the error estimate $O(E^{1/2})$.

To identify modifications to the §1.2.1 results needed on the spin-down time scale $t = O(E^{-1/2})$, we investigate the complete LT of the mainstream radial flow $\overline{u} = (r/\ell)\overline{\mathfrak{u}}$ in the appropriate integral approximation style

$$\widehat{\overline{\mathfrak{u}}}(p) \;=\; \frac{\mathrm{i}E^{1/2}\big[(p-2\mathrm{i})^{1/2}-(p+2\mathrm{i})^{1/2}\big]}{2p(p-2\mathrm{i})^{1/2}(p+2\mathrm{i})^{1/2}-E^{1/2}\big[(p-2\mathrm{i})^{3/2}+(p+2\mathrm{i})^{3/2}\big]} \tag{1.25}$$

(see Oruba *et al.* 2017 equation (A3*a*) with (A2*c*-*e*), and cf. Greenspan & Howard 1963 equation (3.14) albeit in the context of $\widehat{\overline{\mathfrak{v}}}$). As well as the $O(E^{1/2})$ errors already stressed, there are other related limitations on the approach imposed by dependence on time t. The approximation is good at early time $t = O(1)$, consistent with our integral style in §1.2.1 (directed to by the assumption that the $z = 1$ boundary is "far away"), but becomes weaker as time increases. By implication, the formulation (1.25) is valid, provided that the MF boundary layer width $\Delta(t) = \sqrt{Et}$ is small, which limits applicability to

$$t \;\ll\; E^{-1}\,. \tag{1.26}$$

To determine the spin-down QG-part $\overline{\mathfrak{u}}_{QG}$ proportional to

$$\mathfrak{E}(t) \;=\; \exp(-E^{1/2}\sigma t)\,, \tag{1.27a}$$

we need the real pole-location, i.e., the zero of the denominator of (1.25),

$$p \;=\; -\,E^{1/2}\sigma \;=\; -\,2\tan(2\beta_{QG})\,, \tag{1.27b}$$

close to $p = 0$. Here, $\beta_{QG} = O(E^{1/2})$ solves

$$\sin(2\beta_{QG}) \;=\; \tfrac{1}{2}E^{1/2}\,[\cos(3\beta_{QG})+\sin(3\beta_{QG})]\,[\cos(2\beta_{QG})]^{1/2} \tag{1.27c}$$

with the approximate solution

$$\beta_{QG} = \tfrac{1}{4}E^{1/2}\big(1+\tfrac{3}{4}E^{1/2}\big)+O(E) \qquad\Longrightarrow\qquad \sigma \;=\; 1+\tfrac{3}{4}E^{1/2}+O(E)\,. \tag{1.27d,e}$$

Bearing in mind that $\partial\overline{v}_{QG}/\partial t = -2\overline{u}_{QG}$ implies $\overline{u}_{QG} = \frac{1}{2}E^{1/2}\sigma\overline{v}_{QG}$ (use (1.27*a*)) and noting the initial value $\overline{v}_{QG}(0) = \kappa$ (see (1.22*a*)), we see that

$$\overline{\mathfrak{u}}_{\mathfrak{E}}(t) \;=\; \tfrac{1}{2}\sigma\kappa E^{1/2}\,\mathfrak{E}(t) \qquad\qquad (\mathfrak{E}\text{-trigger}) \tag{1.28}$$

correctly describes the early time behaviour of $\overline{\mathfrak{u}}_{QG}(t)$, found in §1.2.1, in agreement with ($\mathcal{O}$: 1.20*a*). Our identification of the factor κ (1.22*c*), as the initial value $\overline{\mathfrak{v}}_{QG}(0)$ (1.22*a*) following the removal of the MF-part $\overline{\mathfrak{v}}_{MF}(0)$ from $\overline{\mathfrak{v}}(0)$ is significant. Previously, Oruba *et al.* (2017) derived κ formally as the residue (their equation (A5*b*)) at the (QG-)pole (1.27*b*) of the LT (1.25), without any physical interpretation.

Curiously, there are two further poles of (1.25) that occur with $p \pm 2\mathrm{i} = O(E)$, very close to the cut-points $p = \mp 2\mathrm{i}$, and so outside the domain $|p \pm 2\mathrm{i}| \gg E$ of validity of (1.25). This condition stems from the requirement that LT boundary layer width of order

$E^{1/2}|p \pm 2\mathrm{i}|^{-1/2}$, as determined by (1.11$a$), is less than the gap width unity. The poles are spurious and not a feature of the complete LT-solution. So, with only $|p \pm 2\mathrm{i}| \gg E$ relevant, a plausible approximation of (1.25), for $t \ll E^{-1}$ (1.26) of interest, is obtained upon setting $E = 0$ in the denominator of its right-hand side

$$\overline{\mathfrak{u}}_{\mathfrak{W}}(t) \,=\, \tfrac{1}{2}E^{1/2}\,\mathfrak{W}(t) \,=\, E^{1/2}\,\mathfrak{U}(t) \qquad (\mathfrak{W}\text{-trigger}). \tag{1.29a}$$

Since $\mathfrak{U}(t) = \mathfrak{U}_{E} + \mathfrak{U}_{MF}(t)$ (see (1.14)–(1.17)), we may partition the $\mathfrak{W}$-trigger flow into

$$\overline{\mathfrak{u}}_{E} \,=\, \tfrac{1}{2}E^{1/2}\,\mathfrak{W}_{E} \,=\, E^{1/2}\,\mathfrak{U}_{E} \,=\, \tfrac{1}{2}E^{1/2} \qquad (\text{E-trigger}), \tag{1.29b}$$

$$\overline{\mathfrak{u}}_{MF}(t) \,=\, \tfrac{1}{2}E^{1/2}\,\mathfrak{W}_{MF}(t) \,=\, E^{1/2}\,\mathfrak{U}_{MF}(t) \qquad (\text{MF-trigger}). \tag{1.29c}$$

Undoubtedly, the $\mathfrak{W}$-trigger flow $\overline{\mathfrak{u}}_{\mathfrak{W}}(t)$ is far better than the $\mathfrak{E}$-trigger flow $\overline{\mathfrak{u}}_{\mathfrak{E}}(t)$, as by construction, it contains the MF-trigger flow $\overline{\mathfrak{u}}_{MF}(t)$ appearing in (1.18a). However, the remaining E-trigger constituent, $\overline{\mathfrak{u}}_{E} = \overline{\mathfrak{u}}_{\mathfrak{W}}(t) - \overline{\mathfrak{u}}_{MF}(t)$, fails to faithfully capture the spin-down of $\overline{\mathfrak{v}}_{QG}$ suggested by the term $-E^{1/2}t$ in (1.22a), but made explicit by the exponential decay of $\overline{\mathfrak{u}}_{\mathfrak{E}}(t)$. To remedy the absence only of the spin-down decay $\mathfrak{E}(t)$ in (1.29a), Greenspan & Howard (1963) proposed the approximation

$$\widehat{\overline{\mathfrak{u}}}_{GH}(p) \,\approx\, p\widehat{\mathfrak{E}}\,\widehat{\overline{\mathfrak{u}}}_{\mathfrak{W}}(p) \,=\, \tfrac{1}{2}\mathrm{i}E^{1/2}(p + E^{1/2}\sigma)^{-1}\big[(p+2\mathrm{i})^{-1/2} - (p-2\mathrm{i})^{-1/2}\big] \tag{1.30a}$$

(cf. their (3.17)), which may be expressed in terms of $\widehat{\mathfrak{W}}^{\pm}$ (1.11b). Whence the inverse-LT is

$$\overline{\mathfrak{u}}_{GH}(t) \,=\, \tfrac{1}{2}E^{1/2}\Big[(1/\aleph^{+})^{1/2}\mathfrak{W}^{+}\big(\aleph^{+}t\big) \,+\, (1/\aleph^{-})^{1/2}\mathfrak{W}^{-}\big(\aleph^{-}t\big)\Big]\,\mathfrak{E}(t) \tag{1.30b}$$

(cf. their (3.19)), in which the argument $\aleph^{\pm}t$ of $\mathfrak{W}^{\pm}$ (1.12a) depends on

$$\aleph^{\pm} \,=\, 1 \pm \tfrac{1}{2}\mathrm{i}E^{1/2}\sigma\,. \tag{1.30c}$$

Our description of (1.30a), as an "approximation", is a generous interpretation. Rather it is a "composite" that captures the behaviour of the LT (1.25) close to the pole (1.27b) and in the neighbourhood of (but not too close to) the cut-points $p = \pm 2\mathrm{i}$. It is not uniformly good elsewhere. Indeed, even the $O(E^{1/2})$ corrections stemming from the factor $\sigma\kappa$ in the $\mathfrak{E}$-trigger are not captured. Such errors do not bother us. However, we do take seriously the $O(E^{1/2})$ contributions to the decay rates, such as $E^{1/2}\sigma$, and later similar frequency corrections, because both describe secular features that accumulate over long time scales. So, where appropriate, we are at pains to keep track of them. In this connection, we stress that, whereas the QG-contribution to $\overline{\mathfrak{u}}_{GH}$ (1.30b) is Ekman damped, the MF-contribution is not, because $\mathfrak{W}^{\pm}_{MF}(\aleph^{\pm}t)\mathfrak{E}(t) = -[f(\aleph^{\pm}T) \pm \mathrm{i}g(\aleph^{\pm}T)]\exp(\mp 2\mathrm{i}t)$ (see (1.16c)). Though Greenspan & Howard (1963) are clear in their text on this matter, their asymptotic formula equation (3.20) (repeated in equations (2.4.1), (2.4.2) of Greenspan 1968) suggests otherwise.

1.3. *Spin-down between two parallel plates bounded at $r^{\dagger} = L$ for $t \ll E^{-1}$*

In this paper we consider the triggered response to blocking of the mainstream radial outflow $\overline{u}$ by an outer boundary at $r = \ell$. In Oruba *et al.* (2020), we ignored the MF-contribution $-\overline{\mathfrak{u}}_{MF}(t)$ to the trigger and simply considered the $\mathfrak{E}$-trigger $\overline{u} = -\overline{\mathfrak{u}}_{\mathfrak{E}}(t)$ caused by blocking the QG flow $(r/\ell)\overline{\mathfrak{u}}_{\mathfrak{E}}(t)$ (see (1.28)) at $r = \ell$. Here, instead, our objective is to identify the response to the complete trigger $-\overline{\mathfrak{u}}(t)$ caused by blocking the entire unbounded $(0 \leqslant r < \infty)$ flow $(r/\ell)\overline{\mathfrak{u}}(t)$.

Since the complete trigger $-\overline{\mathfrak{u}}(t)$ is extremely complicated possessing the LT (1.25), which is not even valid for all p (see §1.2.2), it makes more sense to employ the approximate form $-\overline{\mathfrak{u}}_{GH}(t)$. Though its slow exponential decay identified by $\mathfrak{E}(t)$ in (1.30b)

is a fundamental feature of the QG-spin down, it only influences the triggered waves of frequency ω by an amplitude factor $[1+O(E^{1/2})]$, i.e., the $O(E^{1/2})$ errors that occur on replacing the factors $(\mathrm{i}\omega+E^{1/2}\sigma)^{-1}$, associated with the residues at the poles $p=\mathrm{i}\omega$ in (1.30a), by $(\mathrm{i}\omega)^{-1}$. For our trigger purpose alone, it is therefore consistent to make the approximation $\aleph^{\pm}=1$ in (1.30b,c) and so obtain

$$\overline{\mathfrak{u}}(t) \;=\; [1+O(E^{1/2})]\,\overline{\mathfrak{u}}_{\mathfrak{W}}(t) \qquad \text{for} \qquad 0<t\ll E^{-1}\,. \tag{1.31}$$

On neglecting the $O(E^{1/2})$ error we are left with the so-called $\mathfrak{W}$-trigger $-\overline{\mathfrak{u}}_{\mathfrak{W}}(t)$ (1.29a), used throughout this paper.

The irrelevance of the continual QG exponential decay on the triggered waves has a further implication. It suggests that the early time $t=O(1)$, rather than the spin-down time $t=O(E^{-1})$, behaviour of $\overline{\mathfrak{u}}_{GH}(t)$ (1.30b) has the greatest influence. The upshot is that, on the one hand, $\overline{\mathfrak{u}}_{GH}(t)$ (1.30b) provides a good composite approximation of the unbounded flow $\overline{\mathfrak{u}}(t)$, with LT (1.25), needed in the construction of the complete solution. On the other, $\overline{\mathfrak{u}}_{\mathfrak{W}}(t)$ (1.29a) is adequate to describe the $\mathfrak{W}$-trigger with the $O(E^{1/2})$ error identified in (1.31).

Our appraisal of the subtle issues, which guide us to the choice of (1.29a) for our $\mathfrak{W}$-trigger, substantiate our careful description of the transient Ekman layer (unbounded) in §1.1 and its early time implications for the later spin-down between parallel boundaries in §1.2.1. Though our concern is with events that occur for $t\gg 1$, when the $\mathfrak{E}$-trigger applies, our discussions make clear that wave generation depends on the early time, $t=O(1)$ behaviour. That is only captured correctly on use of the $\mathfrak{W}$-trigger.

A final consideration pertains to our trigger $-\overline{\mathfrak{u}}_{\mathfrak{W}}(t)=-\overline{\mathfrak{u}}_{E}-\overline{\mathfrak{u}}_{MF}(t)$ (1.29) at $r=\ell$, which is assumed to apply over the entire range $0<z\leqslant 1$ with an equal and opposite point sink at $z=0$. Errors ensue because, in reality, the $z=0$ point-sink at $t=0$ expands, in concert, with the boundary layer width $\Delta(t)=\sqrt{Et}$. Thus the ensuing errors from $\overline{\mathfrak{u}}_{E}$ and $\overline{\mathfrak{u}}_{MF}(t)$ are $O(E^{1/2}\overline{\mathfrak{u}}_{E})$ and $O(\Delta(t)\overline{\mathfrak{u}}_{MF}(t))$, respectively. Since $\overline{\mathfrak{u}}_{MF}(t)=O(t^{-1/2}\overline{\mathfrak{u}}_{E})$ in which the factor $t^{-1/2}$ follows from (A 5), the error from both QG and MF parts is the same $O(E^{1/2}\overline{\mathfrak{u}}(t))$. Fortunately, the size of the error coincides with that accepted in (1.31) to justify our use of the $\mathfrak{W}$-trigger.

1.4. *Outline*

The paper is organised as follows:

In §2, we formulate the mathematical problem for the inertial waves, including their internal viscous dissipation when $E\neq 0$, generated by the $\mathfrak{W}$-trigger. We separate the variables by introducing a z-Fourier series (terms labelled m) in §2.1 and an r-Fourier-Bessel series (terms labelled n) in §2.2, where we provide the LT-solution, namely a double-sum generated by individual mn-modes (2.19d).

Since the $\mathfrak{W}$-trigger (1.29a) scales as $E^{1/2}$, so does the wave solution $E^{1/2}\boldsymbol{v}^{\sim}$ in (2.1a) via the trigger boundary condition (2.2) at $r=\ell$. Without viscosity ($E=0$), there is no spin-down and no inertial wave generation. Nevertheless, in the limit $E\downarrow 0$, following the removal of the amplitude factor $E^{1/2}$, the scaled velocity $\boldsymbol{v}^{\sim}$, derived from the LT-inversion in §3, continues to solve the governing equations (2.3). In §3.1, we identify persistent waves linked to the poles of the LT. Moreover in §3.2, extra MF-waves, linked to the cuts of $\widehat{\mathfrak{W}}$ at $p=\pm 2\mathrm{i}$, are revealed. Though the pole/cut combination identifies the characteristics of individual $\boldsymbol{v}^{\sim}_{mn}$-modes, the accumulated consequence of their double-summation is not revealed. So, to shed further light on the matter, we consider, in appendix C, the large aspect ratio case $\ell=L/H\gg 1$, for which a Cartesian approximation of the geometry applies when $\ell-r=O(1)$. We employ the $\ell\gg 1$

asymptotic methods of §$\mathcal{O}$:4.2, which approximates the discrete Fourier-Bessel spectrum j_n/ℓ (see (2.16*a*)) by a continuous wavenumber k. In this way the r-Fourier-Bessel sum over n is approximated by a more amenable Fourier integral over k.

In appendix C.1 (adaption of §$\mathcal{O}$:5) the z-Fourier series is recast as the sum of image systems, generated by z-shifts of a primary solution defined on an unbounded domain $-\infty < z - \infty$. This solution is particularly revealing for moderate $\ell - r$ and t, when the images constitute perturbations of the primary solution. In appendix C.2 (adaption of §$\mathcal{O}$:6), we apply the method of steepest descent (stationary phase) to determine the $t \gg 1$ behaviour of individual z-Fourier m-harmonics, which is useful once the $m = 1$ mode in (2.6) dominates the solution. As the derivations are lengthy and parallel much of Oruba *et al.* (2020), their details have been relegated to appendix C. Nevertheless, the results are important because they explain features of the analytic solution generated by the numerical evaluation of the §3 mn-sums portrayed in panels (*c*) of figures 1–4. Appendix C.1 accounts for the fan-like structures on the right near $r = \ell$, while appendix C.2 identifies the front location on the left, where the waves are attenuated.

The results of §3 and appendix C must, of course, be interpreted within the framework of the limit $E \downarrow 0$ and as such only describe waves in the mainstream, exterior to all boundary layers. Once the MF boundary layer (A 7) has expanded to fill the entire region on the time scale $t = O(E^{-1})$, the solution is no longer applicable, so placing an absolute limit on the usefulness of the solution to the range $0 < t \ll E^{-1}$. Viscous effects are, however, manifest on the spin-down time $t = O(E^{-1/2})$ and even earlier for waves with sufficiently short length scales (internal friction). So, in §4, we address the small but finite-E corrections to the mainstream individual wave amplitudes $\boldsymbol{v}^{\sim}_{mn}$ found previously in §3 by solving the governing equations with $E = 0$. Our remit is restricted to finding $O(E^{1/2})$ decay rates and frequency perturbations due to internal friction in §4.1 and accounting for similar corrections due to Ekman layer damping in §4.3. The transitory nature of the Ekman layers for modes with frequencies close to 2 introduces complications that we accommodate by a composite solution in §4.2, which we argue gives the required low order accuracy for all $t \ll E^{-1}$.

We performed Direct Numerical Simulations (DNS) of the spin-down governing equations subject to the complete boundary conditions for various small values of E, which we discuss in §5. Oruba *et al.* (2020) proposed a Filtered DNS (referred to as FNS), for which the QG-part $\overline{\boldsymbol{v}}_{QG}$ of the complete $\boldsymbol{v}_{DNS}$ was removed. In §5.1 we define a new FNS, whereby the mainstream z-independent MF-part $\overline{\boldsymbol{v}}_{MF}$ is also removed (see (5.4)). This has the advantage, over the previous Oruba *et al.* (2020) definition, that the resulting FNS in the mainstream, exterior to all boundary layers, may be compared directly, in §5.2, with the inertial wave solutions of the triggered wave problem formulated in §2. Comparisons, at $E = 10^{-4}$, $\ell = 10$, are presented in figures 1–4 below. Within the various panels of those figures, we compare the FNS (panels (*a*)) to the analytic results from our new $\mathfrak{W}$-trigger (1.29*a*) for finite E (panels (*b*)) and in the $E \downarrow 0$ limit (panels (*c*)), and our previous $\mathfrak{E}$-trigger (1.28), employed with $\mathfrak{E} = 1$, (panels (*d*)). In making comparisons with the results of Oruba *et al.* (2020), it is important to note that, up to the same order of accuracy achievable by the $\mathfrak{W}$-trigger, the $\mathfrak{E}$-trigger is adequately described by the E-trigger (1.29*b*). Our new $\mathfrak{W}$-trigger solutions are almost identical to the FNS, whereas our previous $\mathfrak{E}$-trigger (essentially the E-trigger) exhibits small amplitude and phase defects. The origin of these defects is explained by various analytic comparisons made in §3.1 and appendix C. A more quantitative assessment of the relative accuracy of the analytic- and FNS-results for our $\mathfrak{W}$-trigger is described in §5.3.

We conclude with an overview in §6.

2. The mathematical problem

Our strategy parallels Oruba *et al.* (2020). So here we draw on their results by referencing the relevant equations but only sketch the methodology; for a more careful appraisal, the reader is referred to that work and references therein (for a general reference to inertial waves in a container, see Zhang & Liao 2017).

The essential idea is that the flow $\boldsymbol{v}_{GH}$ (say) between unbounded parallel planes ($\ell \to \infty$), whose LT-solution is given by equations (3.4)–(3.6) of Greenspan & Howard (1963), provides the lowest order solution to the bounded (ℓ large but finite) problem. The main point, emphasised in §1.3, is that outside boundary layers the horizontal components $\overline{\boldsymbol{v}}_{QG\perp}$ and $\overline{\boldsymbol{v}}_{MF\perp}$ of both the QG and MF-flow contributions (for $\ell \to \infty$), that together comprise $\boldsymbol{v}_{GH\perp}$ (see (2.1*b*)), are z-independent; the small axial components $\overline{w}_{QG}$, $\overline{w}_{MF}$ and their sum $\overline{w}_{GH}$ are, of course, all linear in z. However, the failure of the radial velocities $\overline{u}_{QG} = (r/\ell)\overline{\mathfrak{u}}_{QG}$ and $\overline{u}_{MF} = (r/\ell)\overline{\mathfrak{u}}_{MF}$, both of $O(E^{1/2})$, to meet the requirement $\overline{u}(\ell, t) = 0$ triggers a further inertial wave response $E^{1/2}\boldsymbol{v}^{\sim}$ (referred to as $E^{1/2}\boldsymbol{v}^{wave}$ by Oruba *et al.* 2020). As we are only interested in $\boldsymbol{v}^{\sim}$ outside the Ekman layer (both steady and transient) and side-wall boundary layers, we ignore those boundary layers and write

$$\boldsymbol{v} \approx \overline{\boldsymbol{v}}_{GH} + E^{1/2}\boldsymbol{v}^{\sim}, \qquad \overline{\boldsymbol{v}}_{GH} = \overline{\boldsymbol{v}}_{QG} + \overline{\boldsymbol{v}}_{MF}. \tag{2.1a,b}$$

Our objective is to determine $\boldsymbol{v}^{\sim}$ obtained subject to the $\mathfrak{W}$-trigger boundary condition

$$u^{\sim} = -\mathfrak{U}(t) = -\tfrac{1}{2}\mathfrak{W}(t) \qquad \text{at} \qquad r = \ell \qquad (0 < z \leqslant 1) \tag{2.2}$$

(see (1.29*a*)), with a sink of opposite strength at $z = 0$ to ensure that $\int_0^1 u^{\sim}\,\mathrm{d}z = 0$. It is important to note that the radial flow $\overline{u}_{GH}$ differs from the trigger flow $(r/\ell)\overline{\mathfrak{u}}_{\mathfrak{W}}$, for reasons explained in §1.3.

Throughout this section we drop the superscript '$\sim$' and write $\boldsymbol{v} = [u, v, w]$ ($\leftarrow\!\dashv \boldsymbol{v}^{\sim}$). With $w = r^{-1}\partial(r\chi)/\partial r$ (1.4*d*), the inertial wave problem is: Solve

$$\frac{\partial v}{\partial t} + 2u = E\big(\nabla^2 - r^{-2}\big)v, \qquad u = -\frac{\partial \chi}{\partial z}, \tag{2.3a,b}$$

$$\frac{\partial \gamma}{\partial t} - 2\frac{\partial v}{\partial z} = E\big(\nabla^2 - r^{-2}\big)\gamma, \qquad \gamma = -\big(\nabla^2 - r^{-2}\big)\chi \tag{2.3c,d}$$

((2.3*a*,*c*) are the azimuthal equations of momentum, vorticity respectively) subject to the initial ($t = 0$) conditions

$$v = 0, \qquad \gamma = 0, \tag{2.4a,b}$$

and for $t \geqslant 0$ the reduced boundary conditions

$$r\chi = 0 \qquad \text{at} \qquad r = 0 \qquad (0 < z \leqslant 1), \tag{2.5a}$$

$$r\chi = \tfrac{1}{2}\ell(z-1)\,\mathfrak{W}(t) \qquad \text{at} \qquad r = \ell \qquad (0 < z \leqslant 1), \tag{2.5b}$$

$$\chi = 0 \qquad \text{at} \qquad z = 0,\, 1 \qquad (0 < r < \ell), \tag{2.5c}$$

in which the stress boundary conditions, appearing in (5.2) below, have been ignored.

2.1. *The z-Fourier series*

We seek z-Fourier series solutions of the form

$$\begin{bmatrix} \chi \\ v \end{bmatrix} = -\sum_{m=1}^{\infty} \frac{(-1)^m}{m\pi} \begin{bmatrix} \widetilde{\chi}_m(r,t)\sin\big(m\pi(z-1)\big) \\ \widetilde{v}_m(r,t)\cos\big(m\pi(z-1)\big) \end{bmatrix} \tag{2.6}$$

for which (2.5b), noting

$$\tfrac{1}{2}(z-1) \;=\; -\sum_{m=1}^{\infty}\frac{(-1)^m}{m\pi}\sin(m\pi(z-1)) \qquad (0<z\leqslant 1)\,, \tag{2.7}$$

leads to the boundary condition

$$r\widetilde{\chi}_m \;=\; \ell\mathfrak{W}(t) \qquad \text{at} \qquad r\;=\;\ell\,. \tag{2.8}$$

The LT-solution obtained from ($\mathcal{O}$: 2.16a), following the change $\widehat{\mathfrak{E}}(p)\mapsto\widehat{\mathfrak{W}}(p)$, is

$$\begin{bmatrix}\widehat{\widetilde{\chi}}_m\\ \widehat{\widetilde{v}}_m\end{bmatrix} \;=\; \begin{bmatrix}1\\ 2m\pi/\mathfrak{p}\end{bmatrix}\widehat{\mathfrak{W}}(p)\,\frac{\mathrm{J}_1\big(m\pi qr\big)}{\mathrm{J}_1\big(m\pi q\ell\big)}\,. \tag{2.9a}$$

Here J_1 is the Bessel function, while the functions $\mathfrak{p}=\mathfrak{p}(p)$ and $q=q(\mathfrak{p})=q(\mathfrak{p}(p))$ are determined by the dispersion relation ($\mathcal{O}$: 2.17a–d), which gives them as the solutions of

$$\left.\begin{aligned}\mathfrak{p}^2 \;&=\; -\,4\big/\big(q^2+1\big)\,,\\ \mathfrak{p}\;&=\;p\;+\;(q^2+1)\mathsf{d}_m\end{aligned}\right\} \qquad\Longleftrightarrow\qquad \left\{\begin{aligned}q^2+1\;&=\;-\,4/\mathfrak{p}^2\,,\\ p\;&=\;\mathfrak{p}\;+\;4\mathsf{d}_m/\mathfrak{p}^2\,,\end{aligned}\right. \tag{2.9b,c}$$

where

$$\mathsf{d}_m \;=\; E(m\pi)^2. \tag{2.9d}$$

In terms of the Bessel function of imaginary argument I_1, the initial behaviour

$$\widetilde{\chi}_m \;\approx\; \frac{8t^{3/2}}{3\sqrt{\pi}}\,\frac{\mathrm{I}_1\big(m\pi r\big)}{\mathrm{I}_1\big(m\pi\ell\big)} \qquad (t\ll 1) \tag{2.10}$$

is recovered on expanding the integrand of the inverse-LT $\mathcal{L}^{-1}\big\{\widehat{\widetilde{\chi}}_m\big\}$ of $\widehat{\widetilde{\chi}}_m$ defined by (2.9a) under the limit $p\to\infty$, for which $q\to\mathrm{i}$ (see (2.9c)) and noting that $\mathfrak{W}(t)\approx 8t^{3/2}/(3\sqrt{\pi})$ for $t\ll 1$ (see (1.12a,c)). The initial response (2.10), $\propto t^{3/2}$, is "softer" than the impulsive response ($\mathcal{O}$: 2.9c) to the $\mathfrak{E}$-trigger.

For $t>0$ the LT-inversion of (2.9a) involves consideration of the contributions from various poles, which include the zeros of $\mathrm{J}_1\big(m\pi q\ell\big)$, as well as the cuts at $p=\pm 2\mathrm{i}$ exhibited by $\widehat{\mathfrak{W}}(p)$. Since we have omitted the stress boundary conditions at $r=\ell$, following Oruba *et al.* (2020), we disregard the shear layer responses, both QG and ageostrophic, abutting the outer boundary $r=\ell$ linked to the poles $p=0$ (in $\widehat{\mathfrak{W}}(p)$) and $\mathfrak{p}=0$ (in the factor $\mathfrak{p}^{-1}$ of the expression for $\widehat{\widetilde{v}}_m$). Their proper treatment using the full boundary conditions (5.2) was undertaken by Oruba *et al.* (2017).

To understand the nature of the triggered waves, we begin by focusing attention on the remaining set $\daleth$ of poles $p=p_{mn}$, p^*_{mn} (the superscript '$*$' denotes the complex conjugate) identified by

$$q\;=\;q_{mn}\;=\;j_n\big/(m\pi\ell)\;(>0)\,, \tag{2.11}$$

determined by the real zeros j_n of $\mathrm{J}_1\big(m\pi q\ell\big)$ (i.e., $\mathrm{J}_1(j_n)=0$). In turn, they define

$$\mathfrak{p}_{mn}\;=\;\mathrm{i}\omega_{mn}\,, \qquad\qquad \omega_{mn}\;=\;2\Big/\sqrt{q^2_{mn}+1}\,, \tag{2.12a,b}$$

$$p_{mn}\;=\;\mathrm{i}\omega_{mn}\;-\;d_{mn}\,, \qquad\qquad d_{mn}\;=\;4\mathsf{d}_m\big/\omega^2_{mn}\,, \tag{2.12c,d}$$

and, following the differentiation of $p=\mathfrak{p}+4\mathsf{d}_m/\mathfrak{p}^2$ (2.9c), they determine the value

$$\left[\frac{\mathfrak{p}}{p}\frac{\mathrm{d}p}{\mathrm{d}\mathfrak{p}}\right]_{\mathfrak{p}=\mathfrak{p}_{mn}} \;=\; \frac{\mathrm{i}\omega_{mn}+2d_{mn}}{\mathrm{i}\omega_{mn}-d_{mn}} \qquad \text{at} \qquad p\;=\;p_{mn}\,, \tag{2.12e}$$

needed to evaluate pole residues in §4.1 below. From (2.12b), we may generate

$$\varphi_{mn} \;=\; \sqrt{1-(\omega_{mn}/2)^2} \;=\; \cos(2\alpha_{mn})\,, \tag{2.13a}$$

$$\tfrac{1}{2}\omega_{mn} \;=\; \sqrt{1-\varphi_{mn}^2} \;=\; \sin(2\alpha_{mn})\,, \tag{2.13b}$$

$$q_{mn} \;=\; 2\varphi_{mn}/\omega_{mn} \;=\; \cot(2\alpha_{mn})\,, \tag{2.13c}$$

cf. φ_{mn} with $\varphi_\pm$ in (C 8b) in appendix C.1 below. The role of the aforementioned cuts re-emerges in (2.19) below.

Our disregard of the QG-response linked to the poles $p=0$ and $\mathfrak{p}=0$ has consequences on the boundary values (2.8) of individual triggered waves, which actually satisfy

$$r\widetilde{\chi}_m \;=\; \ell\mathfrak{W}_{\scriptscriptstyle MF}(t) \qquad \text{at} \qquad r \;=\; \ell\,, \tag{2.14}$$

i.e., the oscillatory waves cannot exhibit the steady features of the E-trigger $\ell\mathfrak{W}_{\scriptscriptstyle E}$ constituent (1.29b) (a curiosity noted and explained in the last paragraph of section 2.3 of Oruba *et al.* 2020, in connection with the $\mathfrak{E}$-trigger).

2.2. *The r-Fourier-Bessel series*

As in Oruba *et al.* (2020), we take advantage of the Fourier-Bessel series expansion

$$\frac{\mathrm{J}_1(m\pi qr)}{\mathrm{J}_1(m\pi ql)} \;=\; -\,\frac{1}{2}\sum_{n=1}^{\infty}\frac{q_{mn}^2}{\omega_{mn}^{-2}+\mathfrak{p}^{-2}}\;\frac{\mathrm{J}_1(j_n r/\ell)}{j_n\mathrm{J}_0(j_n)} \qquad \text{on} \qquad 0\leqslant r<\ell\,, \tag{2.15}$$

which follows from ($\mathcal{O}$: A3) on noting that (2.9c), (2.12b) together imply $q_{mn}^2-q^2=4(\omega_{mn}^{-2}+\mathfrak{p}^{-2})$. So we write

$$\begin{bmatrix}\widetilde{\chi}_m\\ \widetilde{v}_m\end{bmatrix} \;=\; \sum_{n=1}^{\infty}\begin{bmatrix}\mathring{\chi}^{\mathsf{d}}_{mn}\\ \mathring{v}^{\mathsf{d}}_{mn}\end{bmatrix}\frac{\mathrm{J}_1(j_n r/\ell)}{j_n\mathrm{J}_0(j_n)} \qquad \text{on} \qquad 0\leqslant r<\ell\,. \tag{2.16a}$$

Here, the superscript 'd', distinguishes our general $\mathsf{d}_m\big(=\;E(m\pi)^2\big)\neq 0$ (2.9d) usage from the $\mathsf{d}_m\downarrow 0$ limit considered in the following §3, where the superscript 'd' will be omitted. It follows that the LT of (2.16a) is determined via

$$\begin{bmatrix}\widehat{\mathring{\chi}^{\mathsf{d}}_{mn}}\\ \widehat{\mathring{v}^{\mathsf{d}}_{mn}}\end{bmatrix} \;=\; -\,2\varphi_{mn}^2\begin{bmatrix}\mathfrak{p}\\ 2m\pi\end{bmatrix}\frac{\mathfrak{p}\,\widehat{\mathfrak{W}}(p)}{\mathfrak{p}^2+\omega_{mn}^2} \tag{2.16b}$$

on substitution of $q_{mn}=2\varphi_{mn}/\omega_{mn}$ (2.13c) into (2.15). An unfortunate feature of the Fourier-Bessel series expansion (2.15) is that it necessarily fails at $r=\ell$, where each eigenfunction $\mathrm{J}_1(j_n r/\ell)$ vanishes. So it is not possible for (2.16a) to satisfy the reduced boundary condition $\widetilde{\chi}_m(\ell,t)=\mathfrak{W}_{\scriptscriptstyle MF}(t)$ (2.14) except in the limiting sense $r\uparrow\ell$. That such a limit is achievable is exemplified by the early time inverse-LT (2.10) of (2.9a).

We express the inverse-LT of (2.16b) as

$$\begin{bmatrix}\mathring{\chi}^{\mathsf{d}}_{mn}\\ \mathring{v}^{\mathsf{d}}_{mn}\end{bmatrix} \;=\; -\,\mathcal{L}^{-1}\bigg\{\varphi_{mn}^2\begin{bmatrix}\mathfrak{p}\\ 2m\pi\end{bmatrix}\frac{\widehat{\mathfrak{W}}(p)}{\mathfrak{p}-\mathrm{i}\omega_{mn}}\bigg\}+\text{c.c.}\,, \tag{2.17}$$

where 'c.c.' denotes complex conjugate. A further reduction of the LT $\widehat{\mathring{v}^{\mathsf{d}}_{mn}}$, exhibited by the right-hand side of (2.17), is possible upon using the partial fraction decomposition

$$\frac{1}{\mathfrak{p}-\mathrm{i}\omega_{mn}} \;=\; \frac{1}{\mathrm{i}\omega_{mn}}\bigg[\frac{\mathfrak{p}}{\mathfrak{p}-\mathrm{i}\omega_{mn}}\;-\;1\bigg]. \tag{2.18}$$

The contribution to the inverse-LT $\mathcal{L}^{-1}\big\{\widehat{\mathring{v}^{\mathsf{d}}_{mn}}\big\}$ from the second term $-1/(\mathrm{i}\omega_{mn})$ is pure imaginary and so when added to its complex conjugate vanishes leaving

$$\begin{bmatrix} \mathring{\chi}^{\mathsf{d}}_{mn} \\ \mathring{v}^{\mathsf{d}}_{mn} \end{bmatrix} = \varphi^2_{mn} \begin{bmatrix} -1 \\ 2\mathrm{i}m\pi/\omega_{mn} \end{bmatrix} \mathfrak{W}^{\mathsf{d}}_{mn}(t) + \text{c.c.}\,, \qquad (2.19a)$$

where $\mathfrak{W}^{\mathsf{d}}_{mn}(t)$ has LT

$$\widehat{\mathfrak{W}}^{\mathsf{d}}_{mn}(p) = \frac{\mathfrak{p}\widehat{\mathfrak{W}}(p)}{\mathfrak{p} - \mathrm{i}\omega_{mn}}\,. \qquad (2.19b)$$

The $\mathfrak{W}^{\mathsf{d}}_{mn}$-notation is motivated by the property $\mathfrak{W}^{\mathsf{d}}_{mn}(t) = \mathfrak{W}(t)$, when $\omega_{mn} = 0$. So employing $\mathfrak{W}(t) = \sum_\pm\{\mathfrak{W}^\pm(t)\} \equiv \mathfrak{W}^+(t) + \mathfrak{W}^-(t)$ (1.12c), we write

$$\mathfrak{W}^{\mathsf{d}}_{mn}(t) = \textstyle\sum_\pm\{\mathfrak{W}^{\mathsf{d}\pm}_{mn}(t)\}\,, \qquad (2.19c)$$

where $\mathfrak{W}^{\mathsf{d}\pm}(t)$ has LT

$$\widehat{\mathfrak{W}}^{\mathsf{d}\pm}_{mn}(p) = \frac{\mathfrak{p}\widehat{\mathfrak{W}}^\pm(p)}{\mathfrak{p} - \mathrm{i}\omega_{mn}} = \frac{\pm\mathrm{i}\,\mathfrak{p}}{p(p\pm 2\mathrm{i})^{1/2}(\mathfrak{p} - \mathrm{i}\omega_{mn})} \qquad (2.19d)$$

on use of (1.11b).

We must stress that our use of the $\mathring{\chi}_{mn}$, $\mathring{v}_{mn}$ notation, though similar in spirit to Oruba *et al.* (2020), differs in detail. For whereas the factor $\mathfrak{F}_{mn} = q^2_{mn}\omega^2_{mn}/2 = 2\varphi^2_{mn}$ appears multiplying $[\mathring{\chi}_{mn}, \mathring{v}_{mn}]$ in ($\mathcal{O}$: 2.23a), we have removed it from (2.16a) including it instead in (2.16b) (cf. ($\mathcal{O}$: 2.23b)).

3. The inviscid limit, $E \downarrow 0$, $d_{mn} = 0$

We investigate the response (2.19a) in the $E \downarrow 0$ limit, for which $\mathfrak{p} = p$ and $\widehat{\mathfrak{W}}^{\mathsf{d}\pm}_{mn}(p)$, defined by (2.19$d$), reduces to

$$\widehat{\mathfrak{W}}^\pm_{mn}(p) = \frac{\pm\mathrm{i}}{(p\pm 2\mathrm{i})^{1/2}(p - \mathrm{i}\omega_{mn})} = \Big(\frac{2}{\varpi^\pm_{mn}}\Big)^{3/2} \widehat{\mathfrak{W}}^\pm\Big(\frac{2}{\varpi^\pm_{mn}}(p - \mathrm{i}\omega_{mn})\Big) \qquad (3.1a)$$

with inverse

$$\begin{aligned} \mathfrak{W}^\pm_{mn}(t) &= \sqrt{2/\varpi^\pm_{mn}}\; \mathfrak{W}^\pm\big(\varpi^\pm_{mn}t/2\big)\, \exp\big(\mathrm{i}\omega_{mn}t\big) \qquad (3.1b)\\ &= \mathfrak{P}^\pm_{mn}\big[\mathrm{S}(T^\pm_{mn}) \pm \mathrm{i}\mathrm{C}(T^\pm_{mn})\big]\, \exp\big(\mathrm{i}\omega_{mn}t\big)\,, \qquad (3.1c)\end{aligned}$$

in which we have used (1.11b), (1.12) and introduced

$$\varpi^\pm_{mn} = 2\pm\omega_{mn}\,, \qquad \mathfrak{P}^\pm_{mn} = \sqrt{2/\varpi^\pm_{mn}}\,, \qquad T^\pm_{mn} = \sqrt{2\varpi^\pm_{mn}t/\pi} = T/\mathfrak{P}^\pm_{mn}\,. \quad (3.1d\text{–}f)$$

We note that the above is a simple adaption of the §1.2.2 result (1.30), following the change of variables $\mathrm{i}E^{1/2}\sigma \mapsto \omega_{m,n}$ and $2\aleph^\pm \mapsto \varpi^\pm_{mn}$.

For $\big[\mathring{\chi}^{\mathsf{d}}_{mn}\,,\, \mathring{v}^{\mathsf{d}}_{mn}\big]$, substitution of (3.1$c$) into (2.19$a$,$c$) yields the value

$$\begin{bmatrix} \mathring{\chi}_{mn} \\ \mathring{v}_{mn} \end{bmatrix} = -2\varphi^2_{mn} \begin{bmatrix} \big(\mathcal{C}_{mn}(t)\cos(\omega_{mn}t) + \mathcal{S}_{mn}(t)\sin(\omega_{mn}t)\big) \\ (2m\pi/\omega_{mn})\,\big(\mathcal{C}_{mn}(t)\sin(\omega_{mn}t) - \mathcal{S}_{mn}(t)\cos(\omega_{mn}t)\big) \end{bmatrix}, \qquad (3.2a)$$

where

$$\big[\mathcal{C}_{mn}(t)\,,\,\mathcal{S}_{mn}(t)\big] = \textstyle\sum_\pm\big\{\mathfrak{P}^\pm_{mn}\big[\mathrm{S}(T^\pm_{mn})\,,\,\mp\mathrm{C}(T^\pm_{mn})\big]\big\}\,. \qquad (3.2b)$$

Hence the complete $E \downarrow 0$ version of the solution (2.6) is determined by (2.16a) with $\big[\mathring{\chi}^{\mathsf{d}}_{mn}\,,\, \mathring{v}^{\mathsf{d}}_{mn}\big]$ given by (3.2a).

This analytic $\mathfrak{W}$-trigger solution has been estimated numerically (by truncating the sums involved). The result is shown on the twelve panels (*c*) of figures 1–4, at instants when the solution is well developed. It differs significantly from the approximate (or reduced) $\mathfrak{E}(\approx \mathrm{E})$-trigger solution of Oruba *et al.* (2020) illustrated in panels (*d*). For, as a comparison of panels (c) and (d) shows, the addition of the MF-trigger to form the complete $\mathfrak{W}(=\mathrm{E}+\mathrm{MF})$-trigger corrects the phase issue apparent when only the $\mathfrak{E}$-trigger is used. To understand how the correction is achieved, we need to consider the large time asymptotic behaviour of the solution, at which stage the wave mechanisms are identifiable. To that end, the $E\downarrow 0$ value $\mathfrak{W}_{mn}(t)=\sum_{\pm}\{\mathfrak{W}^{\pm}_{mn}(t)\}$ of $\mathfrak{W}^{\mathsf{d}}_{mn}(t)$, given by (3.1*b*,*c*), is usefully partitioned into the pole- and cut-contributions of (3.1*a*).

3.1. *The pole-part,* $\urcorner$

On consideration of the explicit form for $\widehat{\mathfrak{W}}^{\pm}_{mn}(p)$, given (3.1*a*) the residue at the pole $p=\mathrm{i}\omega_{mn}$ is determined from (3.1*b*), noting that $\mathfrak{W}^{\pm}_{E}=(\pm\mathrm{i}/2)^{1/2}$ (1.14*b*), as

$$\mathfrak{W}^{\urcorner}_{mn}(t) = \big[(\mathrm{i}/\boldsymbol{\varpi}^{+}_{mn})^{1/2}+(-\mathrm{i}/\boldsymbol{\varpi}^{-}_{mn})^{1/2}\big]\,\exp\big(\mathrm{i}\omega_{mn}t\big) \tag{3.3a}$$

$$= \varphi^{-1}_{mn}\exp\big(\mathrm{i}\omega_{mn}t-\alpha_{mn}\big)\,, \tag{3.3b}$$

in which we have introduced α_{mn} via the relation

$$2\varphi_{mn} = \sqrt{\boldsymbol{\varpi}^{+}_{mn}\boldsymbol{\varpi}^{-}_{mn}} = 2\cos(2\alpha_{mn}) \tag{3.3c}$$

(recall (2.13*a*) and (3.1*d*)). The result (3.3*b*) may be checked by squaring both right-hand sides of (3.3*a*,*b*) and noting (2.13*b*), (3.3*c*). Substitution of (3.3*b*) into (2.19*a*) determines

$$\begin{bmatrix}\mathring{\chi}^{\urcorner}_{mn}\\ \mathring{v}^{\urcorner}_{mn}\end{bmatrix} = -\,2\varphi_{mn}\begin{bmatrix}\cos(\omega_{mn}t-\alpha_{mn})\\ (2m\pi/\omega_{mn})\sin(\omega_{mn}t-\alpha_{mn})\end{bmatrix}, \qquad \begin{cases}1>\varphi_{mn}>0\,,\\ 0<\alpha_{mn}<\pi/4\,.\end{cases} \tag{3.4}$$

Cederlöf (1988) solved this normal mode problem but from a different perspective. At first sight his method appears different to ours, because driving stems directly from the transient Ekman pumping $\mathfrak{W}(t)$ (1.9) (see his equation (5.21) in which the LT-form $\widetilde{F}(s)$ is essentially our $\widehat{\mathfrak{W}}(p)$) and not from the boundary condition at $r=\ell$. Nevertheless, after appropriate variable changes, his solution equation (5.25) follows directly from (3.3*a*) via (2.19*a*), (2.16*a*). He does not, however, introduce the instructive phase angles α_{mn}.

It is interesting to compare the above pole-response $\mathring{\chi}^{\urcorner}_{mn}=-2\varphi_{mn}\cos(\omega_{mn}t-\alpha_{mn})$ to our $\mathfrak{W}$-trigger (1.29*a*), with the corresponding $\mathfrak{E}$-trigger (1.28) response, which from ($\mathcal{O}$: 4.2*a*) is $\mathring{\chi}^{\urcorner\mathfrak{E}}_{mn}=-\frac{1}{2}q^{2}_{mn}\omega^{2}_{mn}\cos(\omega_{mn}t)=-2\varphi^{2}_{mn}\cos(\omega_{mn}t)$. The responses differ by a factor φ_{mn} but coincide when $\varphi_{mn}=1$ ($\alpha_{mn}=0$). That is the QG-limit $\omega_{mn}\downarrow 0$, which occurs as $q_{mn}=j_n/(m\pi\ell)\to\infty$, namely the short radial-r length scale limit ($j_n\gg 1$). As the frequency ω_{mn} increases, φ_{mn} decreases (α_{mn} increases) in concert. Accordingly, relative to $\mathfrak{E}$-trigger response $\mathring{\chi}^{\urcorner\mathfrak{E}}_{mn}$, the phase shifted ($\alpha_{mn}\neq 0$) $\mathfrak{W}$-trigger response $\mathring{\chi}^{\urcorner}_{mn}$ increases in amplitude by a factor $1/\varphi_{mn}$. The increasing trend of the phase shift and mode amplitude terminates as $\varphi_{mn}\downarrow 0$ ($\alpha_{mn}\uparrow\pi/4$). That is the MF-limit $\omega_{mn}\uparrow 2$, which occurs as $q_{mn}\downarrow 0$, namely the short axial-z length scale limit, which is of ever decreasing magnitude

$$\begin{bmatrix}\mathring{\chi}^{\urcorner}_{mn}\\ \mathring{v}^{\urcorner}_{mn}\end{bmatrix} \approx -\,2\sqrt{\boldsymbol{\varpi}^{-}_{mn}}\begin{bmatrix}\cos(2t-\pi/4)\\ m\pi\sin(2t-\pi/4)\end{bmatrix}, \qquad \text{as} \qquad \boldsymbol{\varpi}^{-}_{mn}\downarrow 0\,, \tag{3.5}$$

with $\mathring{\chi}^{\urcorner}_{mn}$ yet large compared to $\mathring{\chi}^{\urcorner\mathfrak{E}}_{mn}$ by the factor $\varphi^{-1}_{mn}\approx 1/\sqrt{\boldsymbol{\varpi}^{-}_{mn}}$. Both the phase shift and increased amplitude of the $m=1$ mode are evident in the well developed solution sufficiently far from the outer boundary $r=\ell$ in $\mathfrak{W}$-panels (*c*) of figures 1–4 below, when compared to the $\mathfrak{E}$-panels (*d*), albeit at $E=10^{-4}$.

3.2. *The cut-part,* $\leftrightarrows$

The remaining cut-contribution $\mathfrak{W}_{mn}(t) - \mathfrak{W}^{\urcorner}_{mn}(t)$ is

$$\mathfrak{W}^{\leftrightarrows}_{mn}(t) \;=\; \textstyle\sum_{\pm}\big\{\mathfrak{W}^{\leftrightarrows\pm}_{mn}(t)\big\}\,, \tag{3.6a}$$

where the results (3.1b) give

$$\mathfrak{W}^{\leftrightarrows\pm}_{mn}(t) \;=\; \sqrt{2/\varpi^{\pm}_{mn}}\;\mathfrak{W}^{\pm}_{\scriptscriptstyle MF}\big(\varpi^{\pm}_{mn}t/2\big)\;\exp\big(\mathrm{i}\omega_{mn}t\big) \tag{3.6b}$$

$$\;=\; -\;\mathfrak{P}^{\pm}_{mn}[f(T^{\pm}_{mn}) \pm \mathrm{i}g(T^{\pm}_{mn})]\exp(\mp 2\mathrm{i}t) \tag{3.6c}$$

on application of (1.16b,c), noting $T^{\pm}_{mn} = (\varpi^{\pm}_{mn}T/2)^{1/2}$ (3.1f) (but cf. (3.1c)). The large $T^{\pm}_{mn}$ asymptotic behaviour $f(T^{\pm}_{mn}) \approx (\pi T^{\pm}_{mn})^{-1/2}$, $g(T^{\pm}_{mn}) \approx 0$ (see (A 4a)) determines

$$\mathfrak{W}^{\leftrightarrows}_{mn}(t) \;\approx\; -\,\varphi^{-2}_{mn}(\pi t)^{-1/2}\big[\cos(2t) - \tfrac{1}{2}\mathrm{i}\omega_{mn}\sin(2t)\big] \qquad \text{for} \qquad T^{\pm}_{mn} \gg 1\,. \tag{3.7}$$

Substitution into (2.19a) yields

$$\begin{bmatrix} \mathring{\chi}^{\leftrightarrows}_{mn} \\ \mathring{v}^{\leftrightarrows}_{mn} \end{bmatrix} \;\approx\; \frac{2}{\sqrt{\pi t}}\begin{bmatrix} \cos(2t) \\ m\pi\sin(2t) \end{bmatrix}, \tag{3.8}$$

similar to (3.5) except for the phase shift $\pi/4$ but notably smaller by a factor $(\pi\varpi^{-}_{mn}t)^{-1/2} \approx \sqrt{2}/(\pi T^{-}_{mn})$ whenever $T^{-}_{mn} \gg 1$.

The simplicity of (3.8) suggests the possibility of constructing from it the large t asymptotic form of the cut-solution. On use of the identity

$$\frac{r}{2\ell} \;=\; -\sum_{n=1}^{\infty}\frac{\mathrm{J}_1(j_n r/\ell)}{j_n\mathrm{J}_0(j_n)}\,, \tag{3.9a}$$

determined from the $q \to 0$ limit of ($\mathcal{O}$: A3), substitution of (3.8) into the r-Fourier-Bessel series (2.16a) yields

$$\begin{bmatrix} \widetilde{\chi}^{\leftrightarrows}_{m} \\ \widetilde{v}^{\leftrightarrows}_{m} \end{bmatrix} \;\approx\; -\,\frac{r}{\ell}\,\frac{1}{\sqrt{\pi t}}\begin{bmatrix} \cos(2t) \\ m\pi\sin(2t) \end{bmatrix} \qquad \text{as} \qquad t \to \infty\,. \tag{3.9b}$$

Substitution into the z-Fourier series (2.6), noting (1.18b), determines

$$\begin{bmatrix} \chi^{\leftrightarrows} \\ v^{\leftrightarrows} \end{bmatrix} \;\approx\; -\,\frac{1}{\sqrt{4\pi t}}\,\frac{r}{\ell}\begin{bmatrix} (z-1)\cos(2t) \\ \sin(2t) \end{bmatrix} \;\approx\; -\,E^{-1/2}\begin{bmatrix} \overline{\chi}_{\scriptscriptstyle MF} \\ \overline{v}_{\scriptscriptstyle MF} \end{bmatrix} \qquad (z>0) \tag{3.10}$$

(see §1.2.1 and (A 5)).

The result (3.10) raises disturbing issues. It suggests that the dominant cut-contribution determines a flow contribution of the same size (but opposite in sign) as the original Greenspan & Howard MF-flow responsible for the MF-trigger. However, because of the discontinuous nature of the Fourier series for $(z-1)$ and 1 at $z=0$ and the Fourier-Bessel series for r at $r=\ell$, the series have to reach extremely large values of m and n to achieve convergence. This is an issue because of the large T^{-}_{mn} requirement $t \gg 1/\varpi^{-}_{mn} = 1/(2-\omega_{mn})$ (see (3.1d) and (3.7)). So at any finite t (however large), it is unclear how good the approximation is. Certainly at the values of t, for which results are reported here, some evidence of an MF-contribution from the cut was evident in tests (not illustrated). However, surprisingly a similar MF-contribution from the poles was also found (again not illustrated), which when combined with the cut-contribution led to their cancellation, i.e., there is no evidence of an MF-contribution in panels (c) of figures 1–4, or for that matter in panels (a), (b) of those figures at small but finite E. The large time MF-issues raised provide a focal point for our discussion of the $\ell \gg 1$ limit in appendix C, which explains the curious cancellation evident in the aforementioned numerical results (not illustrated).

Remarkably, the 'method of images' approach of appendix C.1, identifies immediately the main cut contribution (3.10) that prompted our concerns, via the MF-part $-\mathfrak{U}_{MF}(t)$ of the very first term $-\mathfrak{U}(t)$ on the right-hand side of (C 1a). The role of the poles is subtler, because the estimate $|\mathring{\chi}^{\urcorner}_{mn}| \sim T_{mn}|\mathring{\chi}^{\leftrightarrows}_{mn}|$ below (3.8) suggests that the pole contribution will be even bigger. However, the second term on the right-hand side of final result (C 6b) demonstrates that wave interference must occur reducing the accumulated pole effect to exactly that from the cuts. The fact, that $-\mathfrak{U}_{MF}(t) = O(t^{-1/2})$ is indeed the dominant cut contribution, is established by (C 6c), which shows the remainder to be even smaller $O(t^{-1})$ for $t \gg 1$.

An alternative perspective is gleaned from the steepest descent results of appendix C.2, which for $t \gg 1$ identify two wave families $\widetilde{\chi}_{\pm}$ (C 7). The triggered MF-wave $\widetilde{\chi}_{-}$, characterised by (C 10c,d,f), is only pertinent close to the outer boundary $r = \ell$. There, it remains small compared to the low frequency mode $\widetilde{\chi}_{+}$, characterised by (C 10a,b,e). Of even greater importance is the identification, in the last paragraph of appendix C.2, of a wave front at which the $\widetilde{\chi}_{\pm}$-waves merge and beyond which the waves are evanescent, a feature clearly visible in figures 1–4.

4. Small but finite $0 < E \ll 1$

The amplitude of the $E \downarrow 0$ wave-solution, derived in the previous §3, takes no account of its viscous damping. Such consideration is needed to achieve comparison with the direct numerical simulations, which are necessarily undertaken at finite E. In this section, we rectify that omission.

The complete inversion of the LT (2.19d) to obtain $\mathfrak{W}^{\mathsf{d}\pm}_{mn}(t)$ in the small E limit is formidable. So in this section we simply outline an approximate method that suffices for our purpose. To that end we note that the solution may be partitioned as

$$\mathfrak{W}^{\mathsf{d}\pm}_{mn}(t) \;=\; \mathfrak{W}^{\mathsf{d}\pm\urcorner}_{mn}(t) \,+\, \mathfrak{W}^{\mathsf{d}\pm\leftrightarrows}_{mn}(t)\,, \tag{4.1}$$

where $\mathfrak{W}^{\mathsf{d}\pm\urcorner}_{mn}$ and $\mathfrak{W}^{\mathsf{d}\pm\leftrightarrows}_{mn}$ are the pole- and cut-contributions to the inverse-LT of (2.19d).

4.1. *Pole solution*

The pole-contribution is determined from (2.19d) by the residue

$$\mathfrak{W}^{\mathsf{d}\urcorner\pm}_{mn}(t) \;=\; \left[\frac{\pm\mathrm{i}}{(p\pm 2\mathrm{i})^{1/2}}\,\frac{\mathfrak{p}}{p}\,\frac{\mathrm{d}p}{\mathrm{d}\mathfrak{p}}\,\exp(pt)\right]_{\mathfrak{p}=\mathrm{i}\omega_{mn}} \tag{4.2}$$

of the inverse-LT at $p = p_{mn} = \mathrm{i}\omega_{mn} - d_{mn}$ (2.12c,d), corresponding to $\mathfrak{p} = \mathrm{i}\omega_{mn}$ (2.12a). On use of the expression (2.12e) for $\big[(\mathfrak{p}/p)(\mathrm{d}p/\mathrm{d}\mathfrak{p})\big]_{\mathfrak{p}=\mathrm{i}\omega_{mn}}$ and noting from (3.1d) that $p_{mn} \pm 2\mathrm{i} = \pm\mathrm{i}\boldsymbol{\varpi}^{\pm}_{mn} - d_{mn}$, the residue (4.2) becomes

$$\mathfrak{W}^{\mathsf{d}\urcorner\pm}_{mn}(t) \;=\; \tfrac{1}{2}(1\pm\mathrm{i})\,\mathfrak{P}^{\mathsf{d}\pm}_{mn}\,\exp\big(\mathrm{i}\omega_{mn}t - d_{mn}t\big)\,, \tag{4.3a}$$

where

$$\mathfrak{P}^{\mathsf{d}\pm}_{mn} \;=\; \left(\frac{2}{\boldsymbol{\varpi}^{\pm}_{mn} \pm \mathrm{i}d_{mn}}\right)^{1/2}\,\frac{\omega_{mn} - 2\mathrm{i}d_{mn}}{\omega_{mn} + \mathrm{i}d_{mn}}\,, \tag{4.3b}$$

in which $\mathrm{Re}\big\{(\boldsymbol{\varpi}^{\pm}_{mn} \pm \mathrm{i}d_{mn})^{1/2}\big\} > 0$ as required by analytic continuation on increasing d_{mn} from zero. The decay rate $d_{mn} = 4E(m\pi)^2/\omega^2_{mn}$ (see (2.9d), (2.12d)) is a consequence of internal friction (identified by the first term in equation (4.5) of Zhang & Liao 2008).

4.2. *Composite solution*

To obtain an approximate solution of the full problem, we make the ansatz

$$\mathfrak{W}^{\mathsf{d}\pm}_{mn}(t) \;=\; \mathfrak{P}^{\mathsf{d}\pm}_{mn}\,\mathfrak{W}^{\pm}\big(\varpi^{\pm}_{mn}t/2\big)\,\exp\big(\mathrm{i}\omega_{mn}t-d_{mn}t\big)\,, \tag{4.4a}$$

which has the properties

$$\mathfrak{W}^{\mathsf{d}\pm}_{mn}(t)\to\begin{cases}\mathfrak{W}^{\pm}_{mn}(t) & \text{as} \qquad d_{mn}\to 0\,,\\ \mathfrak{W}^{\mathsf{d}\urcorner\pm}_{mn}(t) & \text{as} \qquad T^{\pm}_{mn}\to\infty\,.\end{cases} \tag{4.4b,c}$$

The former limit (4.4b) is a simple consequence of the fact that $\mathfrak{P}^{\mathsf{d}\pm}_{mn}\to\sqrt{2/\varpi^{\pm}_{mn}}$, as $d_{mn}\downarrow 0$, so recovering the $E\downarrow 0$ result (3.1b). The latter limit (4.4c) applies because $\mathfrak{W}^{\pm}\big(\varpi^{\pm}_{mn}t/2\big)\to\mathfrak{W}^{\pm}_{\scriptscriptstyle E}=\frac{1}{2}(1\pm\mathrm{i})$ (1.14b), as $T^{\pm}_{mn}\to\infty$, leaving the pole-contribution (4.3), i.e., the remaining cut-contribution $\mathfrak{W}^{\mathsf{d}\pm\leftrightarrows}_{mn}(t)$ is assumed negligible in this limit.

Our construction of the composite (4.4a) is in much the same spirit as Greenspan & Howards' unbounded flow composite $\overline{\mathfrak{u}}_{GH}(t)$ (1.30b), i.e., neither is a true asymptotic formula, but instead both capture the dominant flow characteristics.

4.3. *Ekman layer damping*

Consistent with our construction of the composite (4.4a), we implement Ekman damping by replacing the exponential $\exp(\mathrm{i}\omega_{mn}t-d_{mn}t)$ with

$$\exp\big[\mathrm{i}\big(\omega_{mn}+\omega^{E}_{mn}\big)t\;-\;\big(d_{mn}+d^{E}_{mn}\big)t\big]\,, \tag{4.5a}$$

where the frequency and damping increments ω^{E}_{mn} and d^{E}_{mn} adopted are those for pure inertial waves, given by ($\mathcal{O}$: 2.25) (also Kerswell & Barenghi 1995; Zhang & Liao 2008). The increments have the form

$$\begin{bmatrix} d^{E}_{mn}\\ \omega^{E}_{mn}\end{bmatrix}\;=\;\sqrt{\frac{E}{2}}\,\varphi_{mn}\begin{bmatrix}(2-\varphi_{mn})\sqrt{1+\varphi_{mn}}\\ (2+\varphi_{mn})\sqrt{1-\varphi_{mn}}\end{bmatrix}\,, \tag{4.5b}$$

where $\varphi_{mn}=\frac{1}{2}\sqrt{\varpi^{+}_{mn}\varpi^{-}_{mn}}=\sqrt{1-(\omega_{mn}/2)^2}$ (see (3.3c)), as can be verified by squaring both sets of expressions for d^{E}_{mn} and ω^{E}_{mn}, given by (4.5b) and ($\mathcal{O}$: 2.25b).

The oscillatory Ekman layer adjacent to $z=0$, frequency ω_{mn}, has a double layer structure of respective widths

$$\varDelta^{\pm}_{mn}\;=\;\mathfrak{P}^{\pm}_{mn}\sqrt{E}\,, \tag{4.6}$$

where $\mathfrak{P}^{\pm}_{mn}=\sqrt{2/\varpi^{\pm}_{mn}}$ (3.1e) (cf., e.g., Kerswell & Barenghi 1995, equation (2.8)). The two widths are readily identifiable on setting $p=2\mathrm{i}\omega_{mn}$ in the exponential $\exp\big[-E^{-1/2}(p\pm 2\mathrm{i})^{1/2}z\big]$ of the LT-solution (1.11a) for $\mathfrak{z}^{\pm}(z,t)$. In the geostrophic limit $\omega_{mn}=0$ ($\mathfrak{P}^{\pm}_{mn}=1$), the steady Ekman layer width $\varDelta_{\scriptscriptstyle E}=\sqrt{E}$ is recovered. The width

$$\varDelta^{-}_{mn}\;=\;\sqrt{Et_{mn}}\qquad\text{with}\qquad t_{mn}\;=\;(\mathfrak{P}^{-}_{mn})^2\;=\;2/\varpi^{-}_{mn}\;>\;0\,, \tag{4.7a,b}$$

of the broader layer increases indefinitely as $\varpi^{-}_{mn}\downarrow 0$ ($\mathfrak{P}^{-}_{mn}\to\infty$), i.e., $\omega_{mn}\uparrow 2$. So the boundary layers of inertial modes, possessing frequencies close to 2, fill the entire gap $0\leqslant z\leqslant 1$ of the layer.

In addition to the MF-matters associated particularly to the final steady state just discussed, there are also delicate issues concerning how those states are reached. The key feature of the transient evolution of inertial modes is their expanding viscous boundary layer width $\varDelta(t)=\sqrt{Et}$ (1.13). It eventually splits into two parts, each of which ceases to grow at time $t=t^{\pm}_{mn}$ that solves $\varDelta(t)=\varDelta^{\pm}_{mn}$. Since $\varDelta^{-}_{mn}>\varDelta^{+}_{mn}$ with $t^{-}_{mn}>t^{+}_{mn}$, the splitting occurs at $t=t^{+}$, at which the thinner reaches its final width $\varDelta^{+}_{mn}$. For

$t > t^+_{mn}$, the thicker broadens until terminating with width Δ^-_{mn} at $t = t^-_{mn}$. Furthermore, whenever $t^-_{mn} \gg 1$, this time may be longer than the times reached in our numerical investigations. In any event, when either $\Delta^-_{mn} = O(1)$ or $1 \ll t \leqslant O(t^-_{mn})$, the formula (4.5*b*) for d^E_{mn} and ω^E_{mn} ceases to apply. Nevertheless, since (4.5*b*) predicts $d^E_{mn} \to 0$ and $\omega^E_{mn} \to 0$ as $|\omega_{mn}| \uparrow 2$ ($\varphi_{mn} \downarrow 0$), their use in that limit, though inappropriate, ought to be harmless.

The defects, just described are of exactly the same nature as the failure of the Greenspan & Howard (1963) LT-solution (1.25) near the cut-points $p = \pm 2\mathrm{i}$, elucidated in the antepenultimate paragraph of §1.2.2 which ends with the definition (1.29) of the $\mathfrak{W}$-trigger. In short, the failure of both the trigger and the waves pertain to boundary layers that expand to fill the entire domain, and as such are two sides of the same coin.

Our appraisal of the situation indicates that it is impossible to produce asymptotic ($0 < E \ll 1$) results that are justifiable in all space or for all time. As explained, our proposed solution (4.4*a*) modified by (4.5*a*), namely

$$\mathfrak{W}^{E\mathsf{d}\pm}_{mn}(t) = \mathfrak{P}^{\mathsf{d}\pm}_{mn}\,\mathfrak{W}^{\pm}\big(\varpi^{\pm}_{mn}t/2\big)\,\exp\big[\mathrm{i}\big(\omega_{mn} + \omega^E_{mn}\big)t - \big(d_{mn} + d^E_{mn}\big)t\big]\,, \tag{4.8}$$

is weakest for disturbances with $\omega_{mn} \approx 2$. Furthermore, in view of the approximate nature of the $\mathfrak{W}$-trigger (1.29), nothing is gained by using the primitive form $\mathfrak{W}^{\mathsf{d}\pm}_{mn}(t)$ of the damped (internal friction only) wave solution defined by its LT (2.19). We, therefore, simply adopt (4.8). Indeed, despite many approximations, our guiding consideration is to maintain accuracy compatible with our $\mathfrak{W}$-trigger assumption. The very tight comparisons with Direct Numerical Simulation (DNS) reported in the following §5 fully endorse this strategy.

5. The filtered DNS (FNS-)velocity

In §$\mathcal{O}$:3 we presented results from the spin-down obtained by performing Direct Numerical Simulations (DNS) of the full governing equations (2.3) subject to the initial conditions

$$v/r = 1\,, \qquad r\chi = 0 \qquad \text{everywhere at} \qquad t = 0\,, \tag{5.1}$$

and boundary conditions

$$r\chi = \frac{\partial(v/r)}{\partial r} = \frac{\partial w}{\partial r} = 0 \quad \text{at} \quad r = 0 \ \text{ and } \ \ell \quad (0 < z < 1)\,, \tag{5.2a}$$

$$r\chi = \frac{\partial(r\chi)}{\partial z} = v/r = 0 \quad \text{at} \quad z = 0 \qquad (0 < r < \ell)\,, \tag{5.2b}$$

$$r\chi = \frac{\partial^2(r\chi)}{\partial z^2} = \frac{\partial(v/r)}{\partial z} = 0 \quad \text{at} \quad z = 1 \qquad (0 < r < \ell)\,, \tag{5.2c}$$

i.e., the bottom plate is rigid (5.2*b*), whereas the top and side boundaries are stress-free (5.2*a*,*c*). From those results, Oruba *et al.* (2020) described how asymptotics valid for $E \ll 1$, could be used to remove the QG-part $\overline{\boldsymbol{v}}_{QG}$ of the flow external to all boundary layers, leaving what they referred to as the filtered DNS (FNS, §$\mathcal{O}$:3.1). From an analytic point of view, that remaining FNS is the sum of the underlying MF-flow $\overline{\boldsymbol{v}}_{MF}$, described in §§1.2.1, 1.2.2, together with the wave part $E^{1/2}\boldsymbol{v}^{\sim}$ triggered at the outer boundary. To simplify matters, only the $\mathfrak{C}$-triggered wave $E^{1/2}\boldsymbol{v}^{\sim}_{\mathfrak{C}}$ ($= E^{1/2}\boldsymbol{v}^{\mathrm{wave}}$ in ($\mathcal{O}$: 2.1)) was considered by Oruba *et al.* (2020). Here we improve on that simplification by considering the flow more faithfully described by $E^{1/2}\boldsymbol{v}^{\sim}_{\mathfrak{W}}$ (i.e., $E^{1/2}\boldsymbol{v}^{\sim}$ in (2.1*a*)).

5.1. *Our new FNS*

We consider the decompositions

$$\boldsymbol{v} \,=\, \boldsymbol{v}_{QG} \,+\, \boldsymbol{v}_{MF} \,+\, E^{1/2}\boldsymbol{v}^{\sim}\,, \tag{5.3a}$$

$$\boldsymbol{v}_{\perp} \,=\, \overline{\boldsymbol{v}}_{QG\perp} \,+\, \boldsymbol{v}^{\vartriangle}_{QG\perp} \,+\, \overline{\boldsymbol{v}}_{MF\perp} \,+\, \boldsymbol{v}^{\vartriangle}_{MF\perp} \,+\, E^{1/2}\boldsymbol{v}^{\sim}_{\perp} \tag{5.3b}$$

of the entire velocity $\boldsymbol{v}$ and the horizontal velocity $\boldsymbol{v}_{\perp}$. Note that there are also ageostrophic side wall boundary layer contributions adjacent to $r = \ell$, ignored in (5.3*a*,*b*). The z-average of (5.3*b*) yields

$$\langle \boldsymbol{v}_{\perp}\rangle \,=\, \langle \boldsymbol{v}_{QG\perp}\rangle \,+\, \langle \boldsymbol{v}_{MF\perp}\rangle \,+\, O(E)\,, \tag{5.3c}$$

where the wave Ekman layer contribution $\langle \boldsymbol{v}^{\sim}_{\perp}\rangle = O(E^{1/2})$ is included in the $O(E)$ error. As the filter only pertains to the flow outside all boundary layers, we are only interested in the contribution $\overline{\boldsymbol{v}}_{QG\perp} + \overline{\boldsymbol{v}}_{MF\perp} + E^{1/2}\boldsymbol{v}^{\sim}_{\perp}$ to (5.3*b*). Oruba *et al.* (2020) filtered the DNS by simply removing the z-independent QG-contribution $\overline{\boldsymbol{v}}_{QG\perp}$. However, a more useful filter is obtained by removing, in addition, the MF-contribution $\overline{\boldsymbol{v}}_{MF\perp}$, which like $\overline{\boldsymbol{v}}_{QG\perp}$ is z-independent. By this devise we are left with our new filtered horizontal velocity

$$\boldsymbol{v}_{FNS\perp} \,=\, E^{-1/2}\big(\boldsymbol{v}_{DNS\perp} \,-\, \overline{\boldsymbol{v}}_{QG\perp} \,-\, \overline{\boldsymbol{v}}_{MF\perp}\big)\,. \tag{5.4}$$

To evaluate our new filter (5.4), we assume that the needed features of the MF-part of the DNS are

$$E^{-1/2}\overline{\boldsymbol{v}}_{MF\perp} \,\approx\, (r/\ell)\big[\,\mathfrak{U}_{MF}\,,\, \mathfrak{V}_{MF} + \mathfrak{R}_{MF}\,\big]\,, \tag{5.5a}$$

$$E^{-1/2}\langle\boldsymbol{v}_{MF\perp}\rangle \,\approx\, (r/\ell)\big[\,0\,,\, \mathfrak{R}_{MF}\,\big]\,, \tag{5.5b}$$

as given by the analytic results (1.20) and (1.23). Thus with $\boldsymbol{v}_{MF}$ assumed known, we remove it from both sides of (5.3*a*) and so obtain $\boldsymbol{v}_{DNS\perp} - \boldsymbol{v}_{MF\perp} = \boldsymbol{v}_{QG\perp} + E^{1/2}\boldsymbol{v}^{\sim}_{\perp}$ instead of (5.3*b*). Then, as in Oruba *et al.* (2020), we use the recipe implicit in ($\mathcal{O}$: 3.4) and ($\mathcal{O}$: 3.7*a*) to relate $\overline{v}_{QG}$ and $\overline{u}_{QG}$ to $\langle v_{QG}\rangle$:

$$E^{-1/2}\overline{\boldsymbol{v}}_{QG\perp} \,\approx\, \mu^{-1}\big[\,\tfrac{1}{2}\sigma\,,\, E^{-1/2}\,\big]\langle v_{QG}\rangle\,, \tag{5.6a}$$

where $\sigma \approx 1 + \frac{3}{4}E^{1/2}$ (1.27*e*), $\mu \approx 1 - \frac{1}{2}E^{1/2}$. Next, (5.3*c*) determines

$$\langle v_{QG}\rangle \,\approx\, \langle v_{DNS}\rangle \,-\, \langle v_{MF}\rangle \,\approx\, \langle v_{DNS}\rangle \,-\, E^{1/2}(r/\ell)\mathfrak{R}_{MF}\,, \tag{5.6b}$$

on use of (5.5*b*). Substitution of $E^{-1/2}\overline{\boldsymbol{v}}_{MF\perp}$ (5.5*a*) and $E^{-1/2}\overline{\boldsymbol{v}}_{QG\perp}$ (5.6*a*,*b*) into (5.4) then provides an explicit representation of $\boldsymbol{v}_{FNS\perp}$ in terms of $\boldsymbol{v}_{DNS\perp}$ and known analytic results. Finally we note that

$$\chi_{FNS} \,=\, E^{-1/2}\chi_{DNS} \,-\, E^{-1/2}(\overline{u}_{QG} + \overline{u}_{MF})(1-z)\,, \tag{5.7}$$

in which $E^{-1/2}\overline{u}_{QG} \approx \frac{1}{2}(\sigma/\mu)\langle v_{QG}\rangle$ (see (5.6*a*)) and $E^{-1/2}\overline{u}_{MF} \approx (r/\ell)\mathfrak{U}_{MF}$ (see (5.5*a*)).

Following the neglect of $\langle v^{\sim}\rangle = O(E^{1/2})$ and other similar approximations such as the reliability of the trigger itself (see, e.g., (1.31)), we expect the filter values χ_{FNS} (5.7) and v_{FNS} (the azimuthal component of (5.4)) to agree with the analytic predictions for $\chi^{\sim}_{\mathfrak{W}}$ and $v^{\sim}_{\mathfrak{W}}$, with $O(E^{1/2})$ error.

5.2. *FNS-results*

For $E = 10^{-4}$, FNS-solutions (using the new filter described above in §5.1) are compared to those obtained using the analytic results of §§3, 4 in figures 1-4. All figures are arranged in three blocks (each consisting of four panels (*a*)–(*d*)) corresponding to different time instants. We adopt the times employed in figures $\mathcal{O}$:1–$\mathcal{O}$:4, close to which

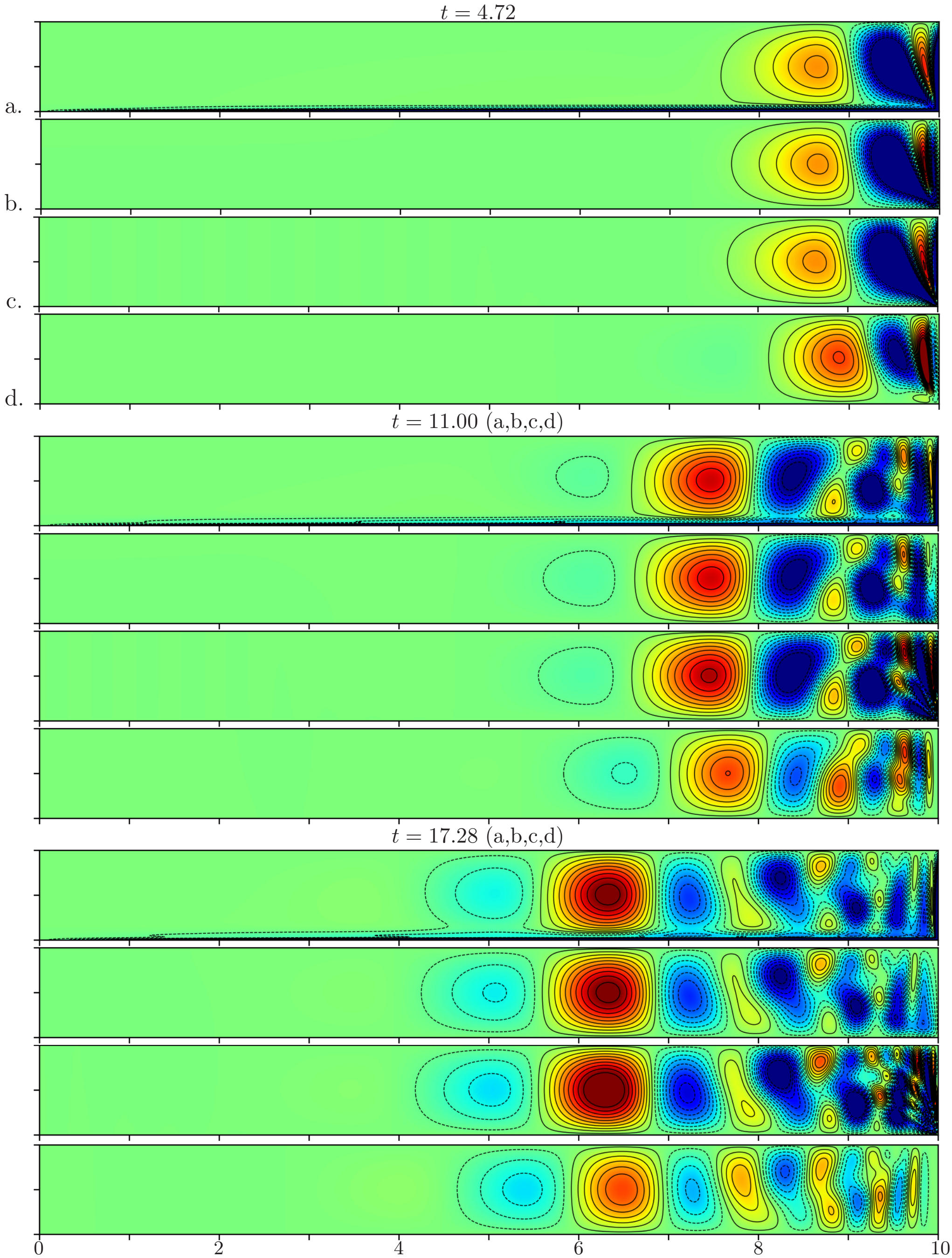

FIGURE 1. The case $E = 10^{-4}$, blocks of $E^{-1/2}\chi$-contours at three distinct instants $t = N\pi/2$ ($N = 3, 7, 11$), namely 4.72, 11.00, 17.28, when $\overline{\chi}_{MF}$ is maximised ($\overline{v}_{MF} \approx 0$). In order, the four panels (a–d) within each block show (a) the filtered-DNS χ_{FNS}; (b) the analytic solution $\chi^{\sim}_{\mathfrak{W}}$ from the new $\mathfrak{W}$-trigger; (c) again $\chi^{\sim}_{\mathfrak{W}}$ but, for comparison, at $E = 0$; (d) the analytic solution $\chi^{\sim}_{\mathfrak{E}}$ from the previous $\mathfrak{E}$-trigger (the z–range is $0 \leqslant z \leqslant 1$; colour scale from -0.1 (blue) to 0.1 (red)).

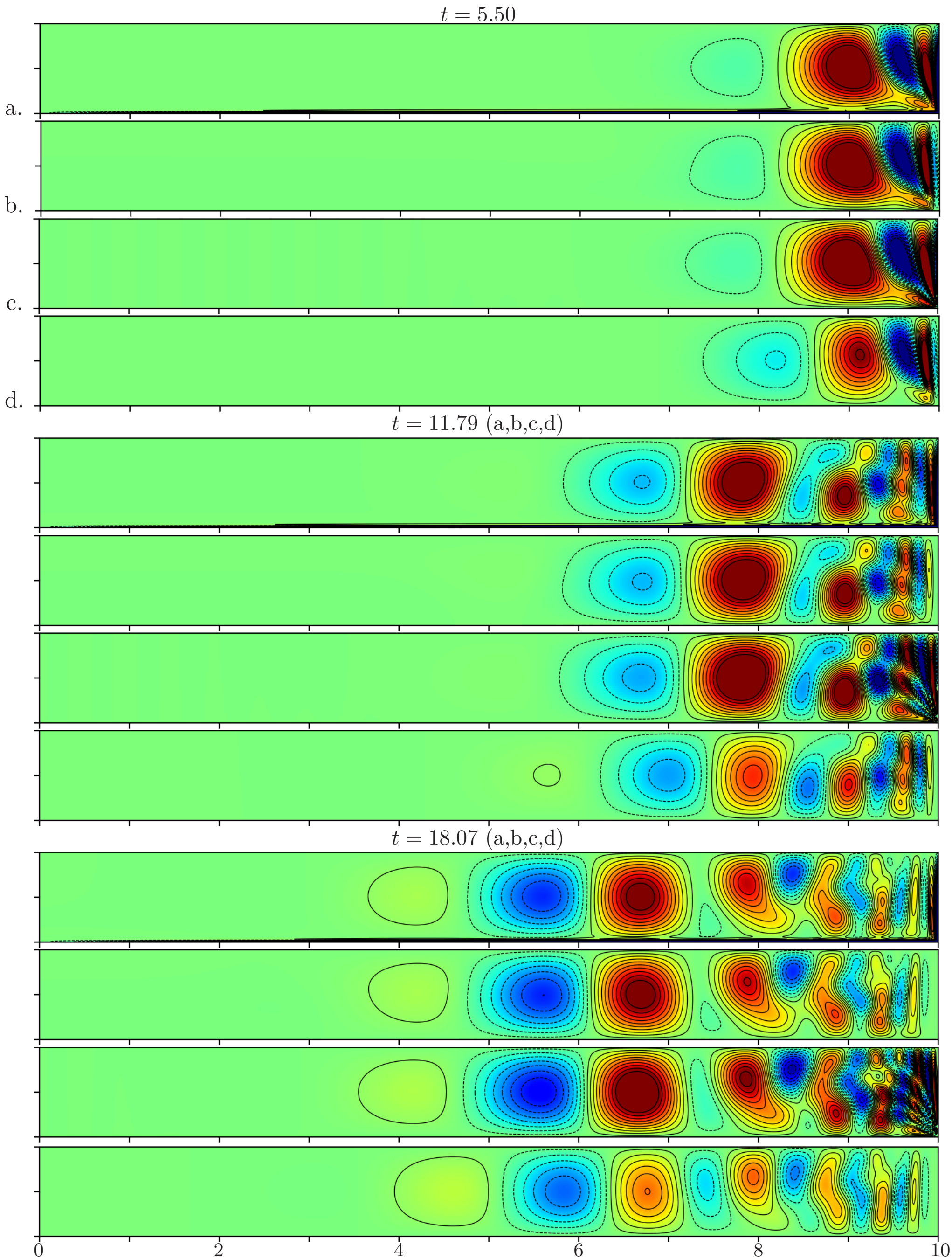

FIGURE 2. As in figure 1 but now at $t = (N + \frac{1}{2})\pi/2$ ($N = 3, 7, 11$), namely 5.50, 11.79, 18.07, when ($\overline{v}_{MF}$ is maximised) $\overline{\chi}_{MF} \approx 0$.

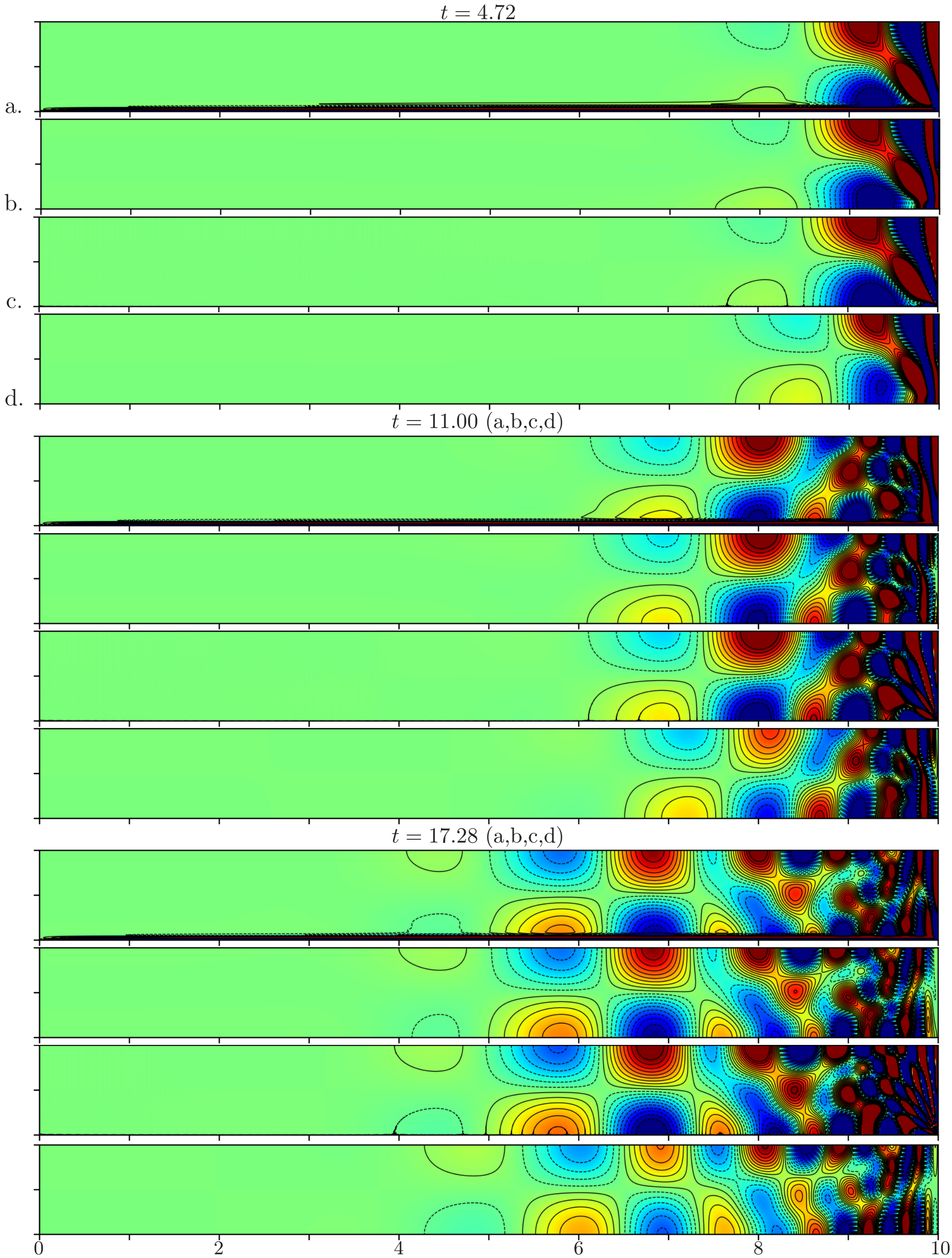

FIGURE 3. As in figure 1, but now $E^{-1/2}v$-contours for the same instants, when ($\overline{\chi}_{MF}$ is maximised) $\overline{v}_{MF} \approx 0$. Each block shows (*a*) the filtered-DNS v_{FNS}; (b) the analytic solution $v^{\sim}_{\mathfrak{W}}$ from the new $\mathfrak{W}$-trigger; (*c*) again $v^{\sim}_{\mathfrak{W}}$ but, for comparison, at $E = 0$; (*d*) the analytic solution $v^{\sim}_{\mathfrak{E}}$ from the previous $\mathfrak{E}$-trigger (the z–range is $0 \leqslant z \leqslant 1$; colour scale from -0.5 (blue) to 0.5 (red)).

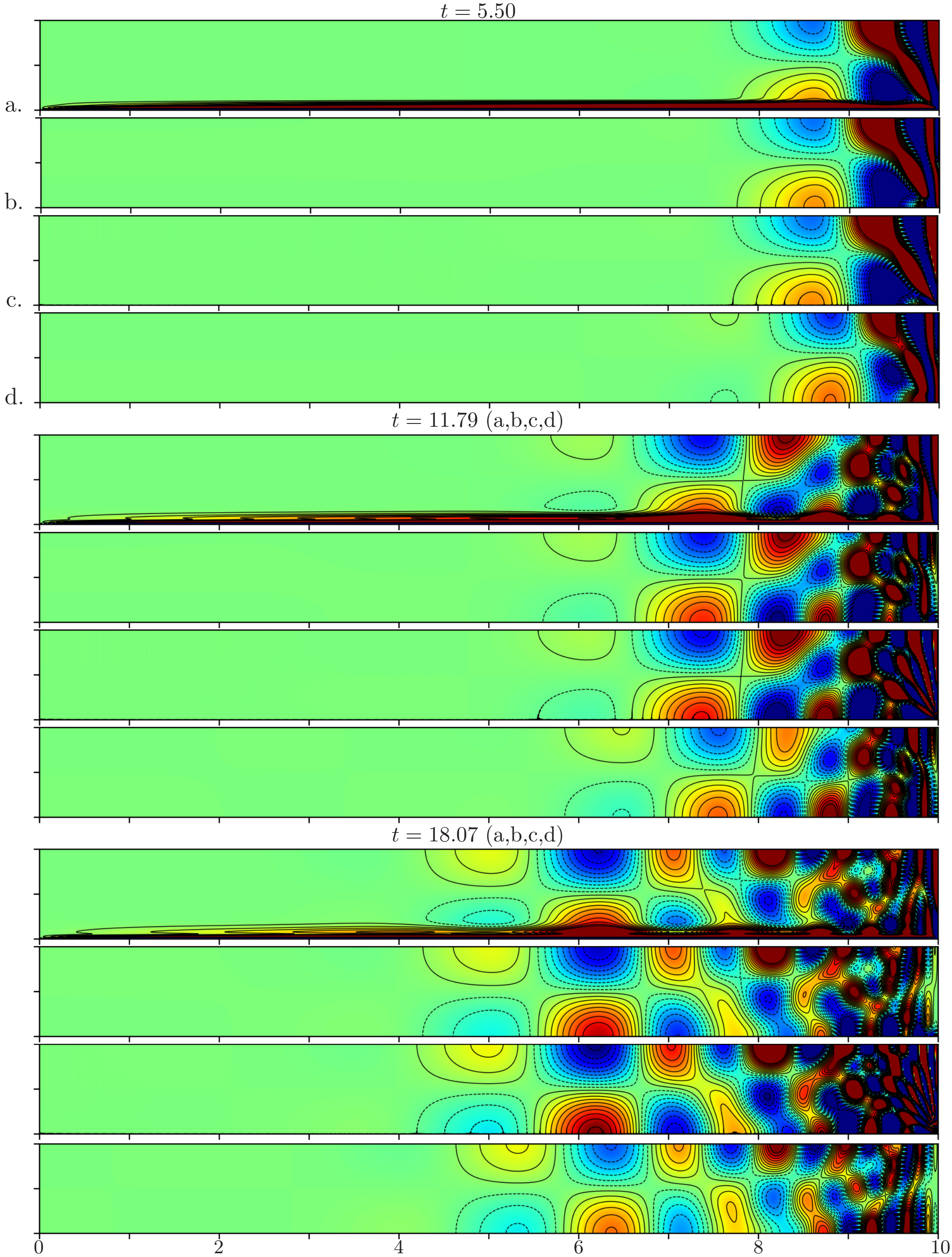

FIGURE 4. As in figure 3 but now at $t = (N + \frac{1}{2})\pi/2$ ($N = 3$, 7, 11), namely 5.50, 11.79, 18.07, as in figure 2, when $\overline{v}_{MF}$ is maximised ($\overline{\chi}_{MF} \approx 0$).

either χ_{MF} or v_{MF} take their stationary values (i.e., the zeros of the time derivative of $\mathfrak{U}_{MF}$ or $\mathfrak{V}_{MF}$ given by (1.17*a*)). As $t \to \infty$, they coincide with the vanishing of the corresponding asymptotic forms (A 5). Though, having filtered out the MF-contribution, those instants are no longer special, we limit our attention to them in order to facilitate comparison of our current $\mathfrak{W}$-trigger results with the earlier $\mathfrak{E}$-trigger results displayed in figures $\mathcal{O}$:1–$\mathcal{O}$:4, albeit for the larger $E = 10^{-3}$. On the one hand, the effects of dissipation are less evident in our $E = 10^{-4}$ figures 1-4. On the other hand and related, our new displays pertain to a very early stage of the spin-down process, i.e., short compared to the QG spin-down time $O(E^{-1/2}) = O(100)$ for $E = 10^{-4}$. As our filter removes the QG flow, the time stage is largely irrelevant to the filter output.

FNS-values for the $\mathfrak{W}$-trigger are portrayed in panel (*a*) of every block. The dark region at the bottom of those panels reflects the Ekman layer (thin and very dark) and the expanding MF shear layer, when present in figures 1, 4 (thicker with some contours visible), that the filter does not remove. There is also an ageostrophic $E^{1/3}$-sidewall Stewartson layer adjacent to the outer $r = \ell$ boundary that the filter does not remove either. Further, it is important to realise that, when the MF-contributions are negligible as in figures 2, 3, the new filter (5.4) is essentially the same as the previous filter. Our $\mathfrak{W}$-triggered wave solution portrayed in panel (*b*) of every block is based on the Ekman layer damped composite solution (4.8). Outside the aforesaid boundary layers, the agreement with panels (*a*) is remarkable. For comparison, we show $\mathfrak{E}$-triggered wave solution, based on the results of Oruba *et al.* (2020) (previously portrayed for $E = 10^{-3}$, but see the following paragraph) in panel (*d*). Though the $\mathfrak{E}$-results identify all the major wave processes involved, the $\mathfrak{E}$-results are clearly found wanting, and, unlike the robust $\mathfrak{W}$-results, do not capture the FNS-solution in detail.

The comparisons just described are all for $E = 10^{-4}$. We can see the effect of changing E from 10^{-3} to 10^{-4} by comparing the FNS, IW (MF+'wave') panels (b), (c) (etc.) of figures $\mathcal{O}$:2, $\mathcal{O}$:3 with our FNS, waves($^{\sim}$) panels (a), (b) (all blocks) of figures 2, 3, because at the instants (with no MF-contribution) chosen the two filters coincide, as do the IW and waves.

In panels (*c*) of figures 1–4, we portray $E = 0$ results obtained by use of (3.1*b*) (equivalently (3.1*c*)), namely the $E = 0$ version of (4.8). Their comparison with panels (*b*) shows how the small dissipation damps the waves. The large scale features are weakly damped, whereas the small scale structures near $r = \ell$ are strongly damped. There further comparison of panels (*b*) with (*a*) shows how well our damping anzatz (4.5) works outside the ageostrophic $E^{1/3}$-sidewall layer, and particularly close to it, where the $E = 0$ panels (*c*) show considerable fan structure, the smoothing of which by dissipation is captured accurately. We mention also that figures $\mathcal{O}$:6, $\mathcal{O}$:7 show the $E = 0$ $\mathfrak{E}$-response that correspond to the $\mathfrak{W}$-results portrayed in panels (*c*) of figures 2, 3. Direct correspondence is not easy. Still, as the $E = 10^{-4}$ results are very similar to the $E = 0$ results except near $r = \ell$, the major differences are simply illustrated in figures 1–4 by comparing the $\mathfrak{W}$-wave results panels (*b*) with the $\mathfrak{E}$-wave results panels (*d*).

Other than the effects of damping, all other features are explained by the $E = 0$ analysis of §3. There we identify the main modification of the $\mathfrak{E}$-wave results of Oruba *et al.* (2020) that lead to our present $\mathfrak{W}$-wave results and so do not repeat them here.

5.3. *Quantitative tests*

In this subsection, our objective is to assess quantitatively how well the FNS is approximated by the analytic $\mathfrak{W}$-triggered wave results on decreasing E. To achieve that goal, we analyse the results for $v_{FNS}(E)$ and $v^{\sim}_{\mathfrak{W}}(E)$ portrayed in the final $t = 18.07$ block of panels (*a*)–(*c*) in figure 4, extending the values of E considered to include $E = 10^{-n}$,

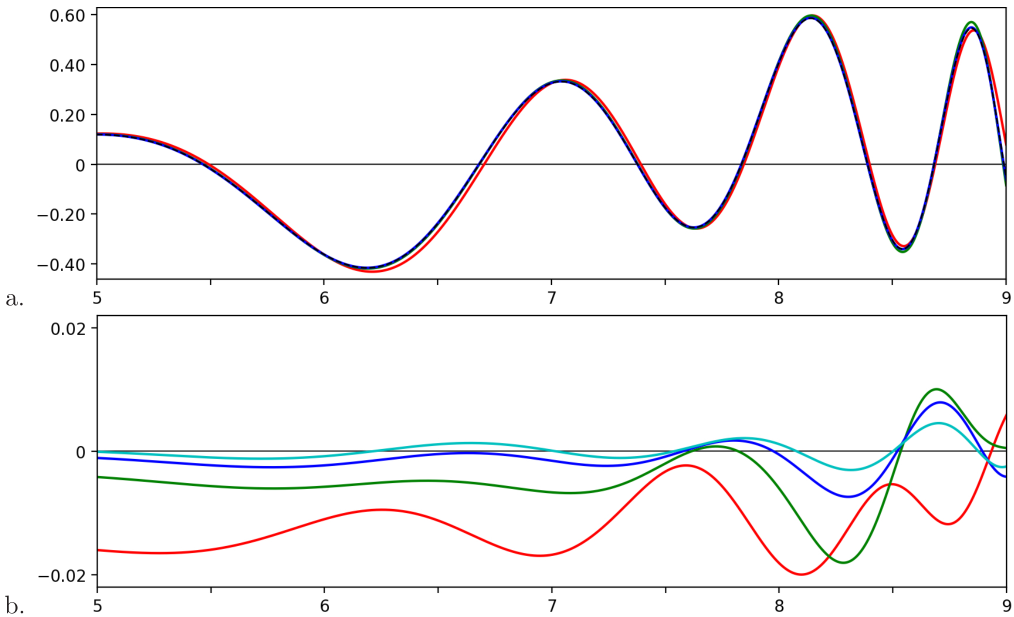

FIGURE 5. Horizontal cross-sections of v–field measures over the range $5 \leqslant r \leqslant 9$ at $z = 0.8$, at $t = 18.07$. (a) shows the linearly interpolated values $v^{\mathrm{lerp}}_{FNS}(E_1, E_2)$ (5.10) that estimate $v_{FNS}(0)$; $(E_1, E_2) = (10^{-3}, 10^{-4})$ (red), $(10^{-4}, 10^{-5})$ (green), $(10^{-5}, 10^{-6})$ (blue). (b) shows the discrepancy $[\![v]\!](E)$ (5.11) between the FNS and $\mathfrak{W}$-trigger solution; $E = 10^{-3}$(red), 10^{-4}(green), 10^{-5}(blue), 10^{-6}(light blue).

$n = 3, 4, 5, 6$. In figures 5 and 6, various quantitative tests are made over the range $5 \leqslant r \leqslant 9$ of significant wave activity, yet outside the $E^{1/3}$-sidewall layer abutting the outer boundary $r = 10$. The height $z = 0.8$ chosen for the horizontal cross-sections is

(i) sufficiently far above the lower boundary $z = 0$ to avoid possible corruption of the results by the tail of the lower $\sqrt{Et}$-MF boundary layer, and

(ii) well inside the upper cells, illustrated in figure 4, in order to capture substantial azimuthal v-wave motion.

The reason for avoiding both the $E^{1/3}$-sidewall and $\sqrt{Et}$-MF boundary layers is that our filter cannot resolve them.

Of particular interest is the $E \downarrow 0$ value of the horizontal FNS-velocity $\boldsymbol{v}_{FNS\perp}(E)$, which being a measure of $E^{1/2}\boldsymbol{v}_{FNS\perp}(E)$, is only defined for $E > 0$. All our estimates suggest that its value is determined analytically by the $E = 0$ value of $\boldsymbol{v}_{\widetilde{\mathfrak{W}}\perp}(E)$ determined by the results (3.2a,b) of §3. So our expectation is that

$$\boldsymbol{v}_{FNS\perp}(0) \equiv \lim_{E\downarrow 0} \boldsymbol{v}_{FNS\perp} = \boldsymbol{v}_{\widetilde{\mathfrak{W}}\perp}(0)\,. \tag{5.8}$$

For $0 < E \ll 1$, various analytic estimates suggest that exterior to all boundary layers $\boldsymbol{v}_{FNS\perp}(E)$ and $\boldsymbol{v}_{\widetilde{\mathfrak{W}}\perp}(E)$ have, at fixed t, expansions of the form

$$\boldsymbol{v}_{FNS\perp}(E) = \boldsymbol{v}_{FNS\perp}(0) + E^{1/2}\boldsymbol{v}'_{FNS\perp} + O(E)\,, \tag{5.9a}$$

$$\boldsymbol{v}_{\widetilde{\mathfrak{W}}\perp}(E) = \boldsymbol{v}_{\widetilde{\mathfrak{W}}\perp}(0) + E^{1/2}\boldsymbol{v}'_{\widetilde{\mathfrak{W}}\perp} + O(E)\,, \tag{5.9b}$$

where the notation $\bullet'$ is intended to suggest $\mathrm{d}\bullet/\mathrm{d}E^{1/2}\big|_{E\downarrow 0}$. As our filter has $O(E^{1/2})$

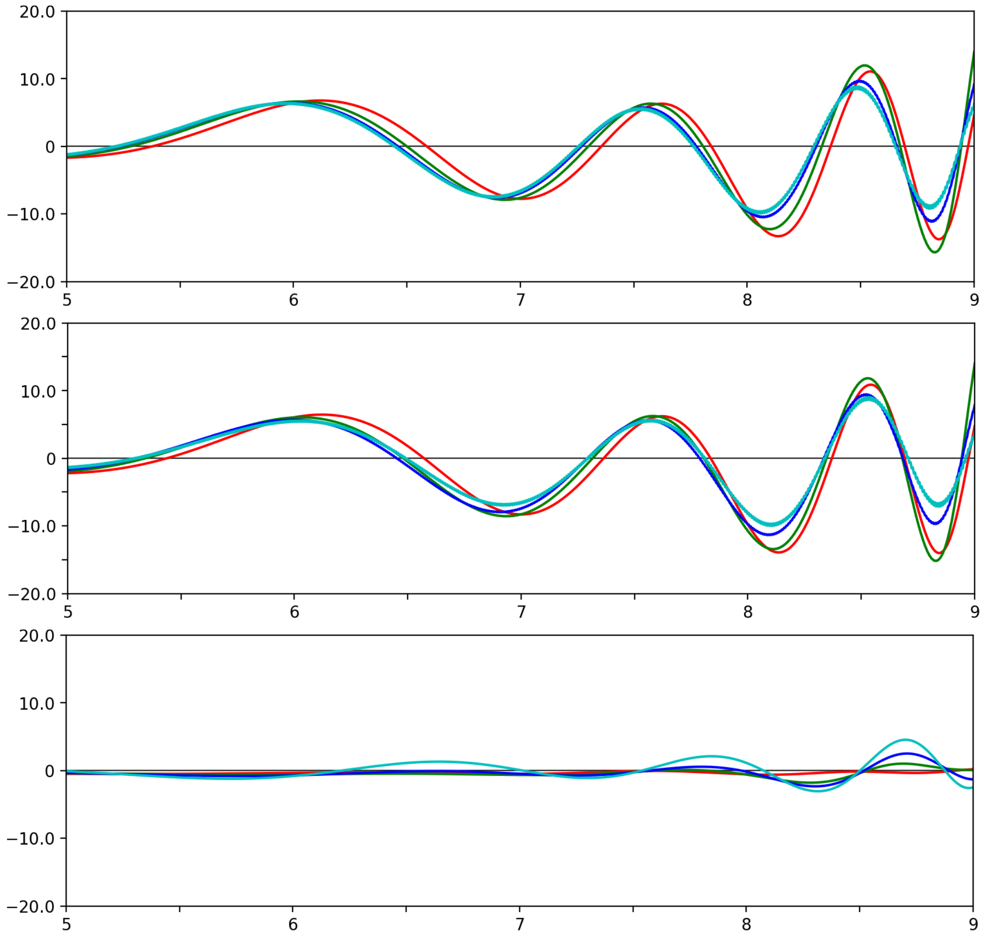

a. b. c.

FIGURE 6. Horizontal cross-sections at $t = 18.07$, as in figure 5, showing the $E^{-1/2}$-scaled (*a*) increment of $v_{\widetilde{\mathfrak{W}}}(E)$, namely $\delta v_{\widetilde{\mathfrak{W}}}(E)/E^{1/2}$ (5.12*a*); (*b*) increment of $v_{FNS}(E)$, namely $\delta v_{FNS}(E)/E^{1/2}$ (5.12*b*); (*c*) difference $[\![v]\!](E)$, namely $[\delta v_{FNS}(E) - \delta v_{\widetilde{\mathfrak{W}}}(E)]/E^{1/2}$ (5.12*c*) (illustrated previously in figure 5(*b*), albeit without the $E^{-1/2}$-scaling).

errors, there is no asymptotic reason for $\boldsymbol{v}'_{FNS\perp}$ and $\boldsymbol{v}'_{\widetilde{\mathfrak{W}}\perp}$ to agree. The main purpose of our tests in figures 5 and 6 is to assess the worth of our ansatz (5.9).

As we cannot determine $v_{DNS}(0)$ (and hence $v_{FNS}(0)$) other than via the limit $E \downarrow 0$, we consider instead its linearly interpolated value

$$v_{FNS}^{\mathrm{lerp}}(E_1, E_2) \equiv \frac{E_2^{1/2} v_{FNS}(E_1) - E_1^{1/2} v_{FNS}(E_2)}{E_2^{1/2} - E_1^{1/2}}, \tag{5.10}$$

which we plot in figure 5(*a*) for various pairs (E_1, E_2). In (5.9), we have been cautious to offer only a two term Maclaurin series. In the unlikely event of the series remaining valid up to the next term $O(E)$, it would follow that $v_{FNS}^{\mathrm{lerp}}(E_1, E_2) = v_{FNS}(0) + O((E_1E_2)^{1/2})$, and then only for sufficiently small E_1 and E_2. Be that as it may, the $v_{FNS}^{\mathrm{lerp}}(E_1, E_2)$ cross-section in figure 5(*a*) converges well. The limiting curve $\boldsymbol{v}_{\widetilde{\mathfrak{W}}\perp}(0)$ is not plotted being indistinguishable to graph plotting accuracy, consistent with our expectation (5.8).

To obtain a measure of the relative sizes of $v'_{\scriptscriptstyle FNS}$ and $v^{\sim}_{\mathfrak{W}}{}'$, we plot in figure 5($b$) the difference

$$[\![v]\!](E) \equiv v_{\scriptscriptstyle FNS}(E) - v^{\sim}_{\mathfrak{W}}(E) = E^{1/2}[v'_{\scriptscriptstyle FNS} - v^{\sim}_{\mathfrak{W}}{}'] + O(E) \tag{5.11}$$

with $O(E)$ error, as estimated by (5.9). Reassuringly $[\![v]\!](E)$ decreases with decreasing E consistent with the implications of convergence in figure 5(a), but not very fast. So in figure 6(c), we plot the scaled value $[\![v]\!]/E^{1/2}$, which by (5.11) ought to tend to an $O(1)$ limit. Instead it shows sign of increasing with decreasing E. It should be emphasised, however, that we are attempting to identify very small effects. For with $v_{\scriptscriptstyle FNS} = O(E^{1/2}v_{\scriptscriptstyle DNS})$, $v'_{\scriptscriptstyle FNS} = O(E^{1/2}v_{\scriptscriptstyle DNS})$, $v^{\sim}_{\mathfrak{W}}{}' = O(E^{1/2}v_{\scriptscriptstyle DNS})$, the relation (5.11) implies that $[\![v]\!] = O(Ev_{\scriptscriptstyle DNS})$, an accuracy which is perhaps hard to achieve from the numerics.

As a further test of the anzatz (5.9) we plot respectively

$$\delta v^{\sim}_{\mathfrak{W}}(E) \equiv v^{\sim}_{\mathfrak{W}}(E) - v^{\sim}_{\mathfrak{W}}(0) = E^{1/2}v'_{\mathfrak{W}} + O(E)\,, \tag{5.12a}$$

$$\delta v_{\scriptscriptstyle FNS}(E) \equiv v_{\scriptscriptstyle FNS}(E) - v^{\sim}_{\mathfrak{W}}(0) = E^{1/2}v'_{\scriptscriptstyle FNS} + O(E)\,, \tag{5.12b}$$

scaled by $E^{-1/2}$ in figures 6(a),(b). There is some evidence that both $\delta v^{\sim}_{\mathfrak{W}}(E)/E^{1/2}$ and $\delta v_{\scriptscriptstyle FNS}(E)/E^{1/2}$ are approaching the proposed respective limiting values $v'_{\mathfrak{W}}$ and $v'_{\scriptscriptstyle FNS}$. To assess this tendency from a slightly different perspective, we plot $[\![v]\!](E)/E^{1/2}$ (5.11) in figure 6(c). Being related to (5.12a,b) via

$$[\![v]\!](E) = \delta v_{\scriptscriptstyle FNS}(E) - \delta v^{\sim}_{\mathfrak{W}}(E)\,, \tag{5.12c}$$

its small size relative to both $\delta v^{\sim}_{\mathfrak{W}}(E)$ and $\delta v_{\scriptscriptstyle FNS}(E)$ is very reassuring, despite lacking evidence of convergence. The lack of convergence may be attributable to the aforementioned numerical error. More seriously, however, the implied presumption that the $O(E^{1/2})$ value of $[\![v]\!](E) = O(E^{1/2})$ defined by (5.11) is meaningful at that order is flawed, because our $\mathfrak{W}$-trigger (1.29), used to obtain $v^{\sim}_{\mathfrak{W}}(E)$, itself possesses $O(E^{1/2})$ errors, as explained in §1.3. Essentially, the accuracy of our $\mathfrak{W}$-trigger is strictly limited and what figure 6(c) attempts to illustrate is beyond the accuracy claimed by our asymptotics. Despite the caveat about figure 6(c), the quantitative measures in figures 5 and 6, strongly support the convergence of the FNS-results as $E \downarrow 0$ to the $E = 0$ analytic results.

6. Concluding remarks

Our present work, when combined with the QG-study of Oruba *et al.* (2017), provides a full analytical solution to the problem of time-dependent motion of a rotating fluid in a plane layer including lateral boundaries, pioneered in the seminal article of Greenspan & Howard (1963). A central feature of our study is the elongated aspect ratio of the domain. In a container with $O(1)$ aspect ratio, inertial wave activity shows little structure and decays rapidly, because waves are quickly reflected at the axis with no time available to create the coherent travelling structures.

The strong inertial wave activity in an elongated domain is likely to have important consequences on the dynamics of large vortices in the atmosphere, such as tropical cyclones. It is indeed quite possible that these waves are associated with the eye-wall replacement (Houze *et al.* 2007; Fischer *et al.* 2020), a feature that is often observed prior to rapid intensifications. To investigate these, the simplified $\mathfrak{E}$-trigger (1.28), essentially equivalent to the E-trigger (1.29b), was adopted by Oruba *et al.* (2020). The triggered waves $\boldsymbol{v}^{\sim}_{\mathfrak{E}}$ obtained within that framework were adequate to explain the main features of the DNS-results.

Here, we extend that preliminary study to include the MF-trigger (1.29c), so constructing the $\mathfrak{W}$-trigger (1.29a). For $E = 10^{-4}$, we find that the comparisons in figures 1–4 of our $\boldsymbol{v}^{\sim}_{\mathfrak{W}}$ predictions based on the faithful $\mathfrak{W}$-trigger (panels (*b*)) with the filtered DNS-waves $\boldsymbol{v}^{\sim}_{FNS}$ (panels (*a*)) are almost perfect in the mainstream above the Ekman layer adjacent to the lower boundary $z = 0$ and away from the ageostrophic $E^{1/3}$-layer abutting outer boundary $r = \ell$. We stress that the comparable $\mathfrak{E}$-trigger results figures $\mathcal{O}$:1–$\mathcal{O}$:4 pertain to the larger value $E = 10^{-3}$ at which diffusive effects are more evident. Only for $E = 10^{-4}$ and smaller is viscosity unambiguously suppressed.

Essentially, relative to Oruba *et al.* (2020), our $\mathfrak{W}$-trigger not only incorporates the E-trigger but the additional MF-trigger as well. Respectively, they take account of the blocking of $\overline{\mathfrak{u}}_E = \frac{1}{2}E^{1/2}$ (1.29*b*) and $\overline{\mathfrak{u}}_{MF}(t) = \frac{1}{2}E^{1/2}\mathfrak{U}_{MF}(t)$ (1.29*c*). The latter (maximum-frequency or) MF-waves are identifiable as such when $t \gg 1$ (Greenspan & Howard 1963). However, for $t \leqslant O(1)$, both $\overline{\mathfrak{u}}_E$ and $\overline{\mathfrak{u}}_{MF}(t)$ are the same size. More strikingly at that early time, the transient Ekman boundary layer flow $\mathfrak{u}(z,t)$ (see (1.6*a*)) exhibits a thin but expanding boundary layer width $\Delta(t) = (Et)^{1/2}$. As the steady Ekman layer part $\mathfrak{u}_E(z)$ (1.15) has width $\Delta_E = E^{1/2}$, the width of the remaining MF boundary layer part $\mathfrak{u}_{MF}(z,t)$ is necessarily the same, in order that the boundary layer width of the sum ($\mathfrak{u} = \mathfrak{u}_E + \mathfrak{u}_{MF}$) is $\Delta(t)$. That is why we remarked in item (ii*b*) (below (1.17)) that "for $t \leqslant O(1)$, the E(or QG)/MF-partition (1.14)–(1.17) is unhelpful". Only for $t \gg 1$ is the representation (A 7) of $\mathfrak{u}_{MF}(z,t)$ truly illuminating.

The above considerations imply that $\overline{\mathfrak{u}}_{\mathfrak{E}}(t)$ and $\overline{\mathfrak{u}}_{\mathfrak{W}}(t)$, which define the $\mathfrak{E}$- and $\mathfrak{W}$-triggers, (1.28*b*) and (1.29*a*) respectively, are distinctly different for $t \leqslant O(1)$, at which stage it is to be expected that the responses to each will also differ. What is surprising is that the difference is not apparent simply at small times but persists, as a comparison of the $E \downarrow 0$ analytic $\boldsymbol{v}^{\sim}_{\mathfrak{W}}$ and $\boldsymbol{v}^{\sim}_{\mathfrak{E}}$ triggered waves, in panels (*c*) and (*d*) respectively of figures 1–4, shows. On the one hand, that comparison shows that the $\mathfrak{E}$-trigger results (panels (*d*)) give a good qualitative description of the wave structure visible in $\boldsymbol{v}_{FNS}$ (panels (*a*) for $1 \gg E > 0$). On the other hand, $\boldsymbol{v}^{\sim}_{\mathfrak{E}}$ (panels (*d*)) suffers a systematic phase-shift and decreased amplitude relative to the true $\boldsymbol{v}^{\sim}_{\mathfrak{W}}$ (panels (*c*)), i.e., the essential differences between the $\mathfrak{E}$- and $\mathfrak{W}$-triggered responses, for $t \gg 1$, are manifest by each wave of given frequency ω_{mn} being 'rung' with different strength and phase by the respective triggers. In the limiting case $E \downarrow 0$, these wave characteristics are identified by the residues of $\widehat{\mathfrak{E}}(p)$ and $\widehat{\mathfrak{W}}(p)$ at the poles $p = \mathrm{i}\omega_{mn}$, as explained in §3.1 with the ideas reinforced by the large ℓ analysis of appendix C (but see particularly (C 7)–(C 9) of appendix C.2). For those reasons alone, our proper consideration of the $\mathfrak{W}$-trigger has yielded a significant improvement over the simpler analysis of the $\mathfrak{E}$-trigger presented in Oruba *et al.* (2020).

Significantly, though $\widehat{\mathfrak{E}}(p)$ only possesses poles, $\widehat{\mathfrak{W}}(p)$ has cut-points as well at $p = \pm 2\mathrm{i}$. In §3.2, we showed that the latter are responsible for wave activity primarily of the MF-type, which appears to cancel Greenspan & Howards' MF-trigger flow. This is an issue, because despite the algebraic decay with time, the MF-trigger flow exists at the times t ($\gg$ 1) illustrated in figures 1 and 4. They are not visible because our new filter has hidden them. However, if we examine the FNS (old filter) and IW panels of the corresponding figures $\mathcal{O}$:1 and $\mathcal{O}$:4, they dominate the wave pattern beyond the triggered wave extent apparent on our new figures 1-4 right up to the axis $r = 0$. In appendix C, we resolved this matter by adopting a Cartesian approximation of the geometry based on $\ell \gg 1$, which applies for $r \gg 1$ up to the outer boundary $r = \ell$. The $t \gg 1$ analysis of appendix C.1 gives the surprising result that the poles provide an accumulated MF-contribution that exactly offsets that due to the cuts. The afore mentioned wave extent is explained and quantified using the method of Coalescing Saddles (see, e.g., the Kelvin's Ship-Wave Pattern https://dlmf.nist.gov/36.13 application of the method) in appendix C.2.

The above remarks about figures 1–4 allude to another matter, namely that they pertain to times t less than the time $t_{\rm axis} = O(\ell)$ taken for the triggered waves to reach the $r = 0$ axis. After that time, wave reflection occurs leading to a confused wave pattern. The ratio of $t_{\rm axis}$ to the spin down time is thus $E^{1/2}\ell$. As we have taken $E = 10^{-4}$, $\ell = 10$ in figures 1–4, for which $E^{1/2}\ell = 10^{-1}$, all those plots correspond to the early spin-down time range $1 \ll t \ll E^{-1/2}$. Upon restricting our times for plots to less than $E^{1/2}\ell$, we need to increase the size of E to obtain a $t = O(E^{-1/2})$ plot time. Indeed the $E = 10^{-3}$ value taken in figures $\mathcal{O}$:1–$\mathcal{O}$:4 is just adequate for that purpose but seriously reduces the accuracy of the asymptotics. As our objective here has been to identify the waves generated with high precision accuracy, we have refrained from following that tack.

Nevertheless, the comparison in figures 1–4 of triggered wave $\boldsymbol{v}^{\sim}_{\mathfrak{W}}$ amplitudes (panels (*b*)) with the FNS $\boldsymbol{v}_{\scriptscriptstyle FNS}$ amplitudes (panels (*a*)), at the same value of E, show subtle improvements over the comparison of $\boldsymbol{v}^{\sim}_{\mathfrak{W}}$ as $E \downarrow 0$ (panels (*c*)) with $\boldsymbol{v}_{\scriptscriptstyle FNS}$. That improvement is particularly striking for the χ-contours of figures 1, 2 just outside the ageostrophic $E^{1/3}$ Stewartson shear layer were the fan structure (see appendix C.1), very evident on panels (*c*), is smoothed out (perhaps for $r \gtrsim 0.95$) on panels (*b*) to provide excellent agreement with panels (*a*). In §5.3 we performed tighter numerical tests on the dependence on E in the range $0.5 \leqslant r \leqslant 0.9$ beyond $r \sim 0.95$, where variation with E is less dramatic. The results portrayed in figures 5 and 6 provide evidence indicating that our analytic treatment of dissipation effects encapsulated by (4.8), which captures the secular viscous wave decay predicted by (4.5), works extremely well for $t \gg 1$.

Of course, a comparison with experimental data would be very rewarding. However, that needs a spin-down experiment (as yet not performed), with a weak forcing to provide a near linear flow, and an elongated aspect ratio, essential to prevent early reflections.

Finally, it is worth reflecting on how our asymptotic approach would compare to an analytic solution $\boldsymbol{v}(r, z, t)$ of the governing equations (2.3) subject to the initial (5.1) and boundary (5.2) conditions, as used by the DNS described in §5. Consider such an LT-solution $\widehat{\boldsymbol{v}}(r, z, p)$. Presumably its LT-inversion simply involves the residues at poles just like those for the unbounded $\ell \to \infty$ case given by equations (3.4), (3.5) of Greenspan & Howard (1963). The poles near $p = 0$ would define the slow spin-down, while the others would define damped waves, each with distinct spatial structure and decay rate. However, as our objective is to determine the overall structure, that emerges, when $t \ll E^{-1}$, on superposing all modes, such an approach is unenlightening for the same reasons that it was abandoned by Greenspan & Howard (1963). The price paid by their asymptotics is the introduction of cuts that do not exist in the original problem. Our approach inherits the consequences of those cuts which are reflected by the character of our $\mathfrak{W}$-trigger. However, for $t \gg 1$, the cut influence decays algebraically with time and a modal structure emerges. What remains are the pole modes with frequencies ω_{mn} (3.4) in §3.1, which are modified to $\omega_{mn} + \omega^E_{mn}$ and damped by the rates $d_{mn} + d^E_{mn}$ given by (4.5) in §4.3. All the disturbing cut issues evaporate as time proceeds. In short, our asymptotics has correctly identified the persistent (i.e., dominant) inertial waves generated, together with their amplitudes over the spin-down time $t = O(E^{-1/2})$.

Appendix A. The transient Ekman MF-layer of §1.1

The transient Ekman layer problem is outlined in §2.3 of Greenspan (1968). There he provides the solution, equations (2.3.4), (2.3.5), of the governing equations (2.3.1)–(2.3.3). His function $F(z, t)$ (equation (2.3.6)) is simply our MF-function $\mathrm{i}\mathfrak{z}^{-}_{\scriptscriptstyle MF}(z, t)$ (see

(1.16a)), more specifically

$$\mathfrak{z}^{\pm}_{MF} = \frac{\mp\mathrm{i}}{2}\biggl[\exp[(1\pm\mathrm{i})E^{-1/2}z]\,\mathrm{erfc}\left(\frac{z}{\sqrt{4Et}} + (1\pm\mathrm{i})t^{1/2}\right) \\ - \exp[-(1\pm\mathrm{i})E^{-1/2}z]\,\mathrm{erfc}\left(-\frac{z}{\sqrt{4Et}} + (1\pm\mathrm{i})t^{1/2}\right)\biggr]. \qquad \text{(A 1)}$$

Put another way, in the LT-inversion of $\widehat{\mathfrak{z}}^{\pm}$ to obtain $\mathfrak{z}^{\pm} = \mathfrak{z}^{\pm}_{E} + \mathfrak{z}^{\pm}_{MF}$, the steady E-part $\mathfrak{z}^{\pm}_{E}$ (1.14a) stems from the pole at $p = 0$, whereas the MF-contributions $\mathfrak{z}^{\pm}_{MF}$ (1.16a) originate from the cut contributions about $p = \mp 2\mathrm{i}$.

The formula (A 1) is at first sight unenlightening. However, in the $t \gg 1$ limit for which the E/MF-partition is useful, the result may be interpreted on use of the formula

$$\mathrm{erfc}\,(\zeta) = \mp\mathrm{i}(1\pm\mathrm{i})\left[f\left(\frac{2\zeta}{(1\pm\mathrm{i})\sqrt{\pi}}\right) \pm \mathrm{i}g\left(\frac{2\zeta}{(1\pm\mathrm{i})\sqrt{\pi}}\right)\right]\exp\bigl(-\zeta^2\bigr) \qquad \text{(A 2)}$$

obtained by reorganising (http://dlmf.nist.gov/7.5.E10). Here the auxiliary functions f, g were introduced in (1.16c) and defined below it. Application of (A 2) to (A 1), with ζ taking its respective values in the first and second lines, leads to the representation (1.16a) with

$$\mathfrak{h}^{\pm}_{MF} = -\tfrac{1}{2}(1\pm\mathrm{i})\Bigl[\bigl[f(T+Z^{\pm}) - f(T-Z^{\pm})\bigr] \pm \mathrm{i}\bigl[g(T+Z^{\pm}) - g(T-Z^{\pm})\bigr]\Bigr], \qquad \text{(A 3}a\text{)}$$

where $T(t) = \sqrt{4t/\pi}$ (1.12b) and

$$Z^{\pm} = \frac{z}{(1\pm\mathrm{i})\sqrt{\pi E t}}\,. \qquad \text{(A 3}b\text{)}$$

Henceforth in this appendix, we restrict attention to the large-t limit, equivalently

$$T \gg 1\,, \qquad \text{(A 4}a\text{)}$$

for which equations (7.12.2/3) of §http://dlmf.nist.gov/7.12.ii give the asymptotic expansions

$$\begin{bmatrix} f(T) \\ g(T) \end{bmatrix} = \frac{1}{\pi T}\begin{bmatrix} 1 \\ (\pi T^2)^{-1} \end{bmatrix}[1 + O(T^{-4})] \approx \frac{1}{\sqrt{4\pi t}}\begin{bmatrix} 1 \\ (4t)^{-1} \end{bmatrix}. \qquad \text{(A 4}b\text{)}$$

Their use in (1.17a) determines

$$\begin{bmatrix} \mathfrak{U}_{MF}(t) \\ \mathfrak{V}_{MF}(t) \end{bmatrix} \approx \frac{1}{\sqrt{4\pi t}}\begin{bmatrix} -\cos(2t) \\ \sin(2t) \end{bmatrix} \qquad \text{(A 5)}$$

in which we have made the approximations $f(T) \approx (\pi T)^{-1}$ and $g(T) \approx 0$.

To identify the MF boundary layer structure defined by $\mathfrak{z}^{\pm}_{MF}(z,t)$, we assume that $Z^{\pm} = O(1)$ with the implication that

$$|Z^{\pm}| \ll T\,. \qquad \text{(A 6}a\text{)}$$

Accordingly, a Taylor series expansion of (A 3a) determines

$$\mathfrak{h}^{\pm}_{MF} \approx -(1\pm\mathrm{i})Z^{\pm} f'(T) \approx \frac{z}{4t\sqrt{\pi E t}}\,, \qquad \text{(A 6}b\text{)}$$

where the prime denotes derivative and $Z^{\pm}$ is given by (A 3b). Substitution of (A 6b) into (1.16a) and use of (1.10a) determines

$$\begin{bmatrix} \mathfrak{u}_{MF} \\ \mathfrak{v}_{MF} \end{bmatrix} = \tfrac{1}{2}\begin{bmatrix} \mathfrak{z}^{+}_{MF} + \mathfrak{z}^{-}_{MF} \\ (\mathfrak{z}^{+}_{MF} - \mathfrak{z}^{-}_{MF})/\mathrm{i} \end{bmatrix} \approx \frac{z}{4t\sqrt{\pi E t}}\begin{bmatrix} \cos(2t) \\ -\sin(2t) \end{bmatrix}\exp\left[-\frac{z^2}{4Et}\right]. \qquad \text{(A 7)}$$

Appendix B. The mean azimuthal MF-flow $\overline{\mathfrak{v}}_{MF}(t)$ for $t = O(1)$

After various integrations of (1.22b) by parts, using the integral representation of $\mathfrak{U}_{MF}$ in the first equality of (1.17a), we may write

$$E^{-1/2}\overline{\mathfrak{v}}_{MF} \approx 2\int_t^\infty \mathfrak{U}_{MF}\,\mathrm{d}t = \mathfrak{V}_{MF} + \mathfrak{R}_{MF}, \tag{B 1a}$$

where

$$\mathfrak{R}_{MF} = -t\left(\frac{\mathrm{d}\mathfrak{V}_{MF}}{\mathrm{d}t} + 2\mathfrak{U}_{MF}\right) - \tfrac{1}{2}\mathfrak{V}_{MF}, \tag{B 1b}$$

in which $\mathrm{d}\mathfrak{V}_{MF}/\mathrm{d}t = (\pi t)^{-1/2}\cos(2t)$. Together they may be employed to establish that the z-average $\langle v_{MF}\rangle = \langle \overline{v}_{MF}\rangle + \langle \mathfrak{v}^{\vartriangle}_{MF}\rangle$ of the azimuthal MF-flow is given by

$$(\ell/r)\langle v_{MF}\rangle \approx \overline{\mathfrak{v}}_{MF} + \int_0^\infty \mathfrak{v}^{\vartriangle}_{MF}\,\mathrm{d}z = \overline{\mathfrak{v}}_{MF} - E^{1/2}\mathfrak{V}_{MF} = E^{1/2}\mathfrak{R}_{MF}. \tag{B 2a}$$

It decays rapidly

$$\mathfrak{R}_{MF} \approx -\frac{\cos(2t)}{8\sqrt{\pi}\,t^{3/2}} = O\big(\mathfrak{V}_{MF}/t\big), \qquad \text{for} \quad t \gg 1 \tag{B 2b}$$

showing that $E^{-1/2}\overline{\mathfrak{v}}_{MF}/\mathfrak{V}_{MF} \to 1$ as $t \to \infty$, which establishes the estimates (1.24).

Appendix C. The Cartesian limit, $\ell = L/H \gg 1$, $\ell - r = O(1)$, for $E \downarrow 0$

In this appendix, to obtain a better understanding of the §3 results, we implement the $\ell \gg 1$ asymptotics of §$\mathcal{O}$:4 that approximates the outer cylindrical geometry as Cartesian and approximates the discrete values j_n/ℓ (see (2.11)) by a continuous wavenumber k. Thus, Fourier-Bessel sums become Fourier integrals, i.e., $\sum_n \mapsto \int \mathrm{d}n$.

C.1. *The 'method of images'*

As in §$\mathcal{O}$:5, we focus attention on the radial velocity u expressed in the form

$$u \approx -\mathfrak{U}(t) + \sum_{-\infty}^{\infty} \breve{u}_l, \qquad \breve{u}_l(x,z,t) = \breve{u}(x, z-2l, t), \qquad x = \ell - r\,(\ll \ell), \tag{C 1a–c}$$

similar to ($\mathcal{O}$: 5.1a,b), and, as in ($\mathcal{O}$: 5.2a,b), introduce the unit vector

$$[x,z]/\varpi = [\mathsf{x},\mathsf{z}] = [\sin(2\alpha), \cos(2\alpha)], \qquad \varpi = \sqrt{x^2+z^2}. \tag{C 2a,b}$$

We multiply the right-hand side of the expression for the LT $\widehat{\breve{u}}$ in ($\mathcal{O}$: 5.2e) by $p\widehat{\mathfrak{W}}(p)$ to obtain, following algebra that utilises the curious but simple identity

$$\frac{\mathsf{x}_\pm}{p-2\mathrm{i}\mathsf{x}} - \frac{\mathsf{x}_\mp}{p+2\mathrm{i}\mathsf{x}} = \pm 2\mathsf{x}\,\frac{p \pm 2\mathrm{i}}{p^2+4\mathsf{x}^2}, \qquad \mathsf{x}_\pm = 1 \pm \mathsf{x}, \tag{C 3a,b}$$

the LT

$$(\pi\varpi)\widehat{\breve{u}} = \tfrac{1}{2}\textstyle\sum_\pm \big\{\mp \mathsf{x}_\pm^{-1/2}\widehat{\mathfrak{W}}^\pm\big((p-2\mathrm{i}\mathsf{x})/\mathsf{x}_\pm\big)\big\} + \text{c.c.}(p \text{ real}). \tag{C 3c}$$

Its LT-inverse, namely the primary $l = 0$ mode (see (C 1b)) to our $\mathfrak{W}$-trigger, is

$$(\pi\varpi)\breve{u} = \tfrac{1}{2}\textstyle\sum_\pm \big\{\mp \mathsf{x}_\pm^{1/2}\mathfrak{W}^\pm(\mathsf{x}_\pm t)\big\}\exp(2\mathrm{i}\mathsf{x}t) + \text{c.c.}, \tag{C 3d}$$

where (C 3c,d) bear a striking structural similarity to (3.1a,b) after linking ω_{mn} to $2\mathsf{x}$. On partitioning $\mathfrak{W}^\pm$ into its pole ⌉: $\mathfrak{W}^\pm_E = \frac{1}{2}(1 \pm \mathrm{i})$ (1.14b) and cut ⇆: $\mathfrak{W}^\pm_{MF}$ (1.16b,c)

parts, we may extract the associated $\breve{u}^{\urcorner}$ and $\breve{u}^{\leftrightarrows}$ of $\breve{u}$ from (C 3d), namely

$$(\pi\varpi)\breve{u}^{\urcorner} = \tfrac{1}{2}\textstyle\sum_\pm\{\mathsf{x}_\pm^{1/2}\}\sin(2\mathsf{x}t) - \tfrac{1}{2}\textstyle\sum_\pm\{\pm\mathsf{x}_\pm^{1/2}\}\cos(2\mathsf{x}t) = \sin(2\mathsf{x}t-\alpha)\,, \qquad (\mathrm{C}\,4a)$$

$$(\pi\varpi)\breve{u}^{\leftrightarrows} = O(t^{-3/2}) \qquad \text{for} \qquad t \gg 1\,, \qquad (\mathrm{C}\,4b)$$

following the surprising cancellation of the $O(t^{-1/2})$ terms. For $t = O(1)$, the contribution $\breve{u}^{\leftrightarrows}$ is complicated but, as (C 4b) shows, decays rapidly for $t \gg 1$.

The previous $\mathfrak{E}$-triggered radial velocity $\breve{u}^{\urcorner\mathfrak{E}}$, namely the so-called mainstream part denoted by $\breve{u}_{ms}$ in ($\mathcal{O}$: 5.6a), is determined using ($\mathcal{O}$: 5.6b) as

$$(\pi\varpi)\breve{u}^{\urcorner\mathfrak{E}} = |\mathsf{z}|\sin(2\mathsf{x}t) = |\varphi|\sin(2\mathsf{x}t)\,, \qquad \varphi \equiv \mathsf{z} = \cos(2\alpha). \qquad (\mathrm{C}\,5)$$

Hence our new $\mathfrak{W}$-triggered $\breve{u}^{\urcorner}$ given by (C 4a), exhibits the same fan-structure near the outer corner $(r,z) = (\ell,0)$, visible in our figures 1-4, as previously identified for $\breve{u}^{\urcorner\mathfrak{E}}$ (C 5) by Oruba *et al.* (2020). Moreover, relative to $\breve{u}^{\urcorner\mathfrak{E}}$, our new $\breve{u}^{\urcorner}$ is characterised by both the amplitude increase φ^{-1} and phase shift α, similar to that described above (3.5) for individual mn-modes.

For $t \gg 1$, the small size of the remaining cut-contribution $\breve{u}^{\leftrightarrows} = O(t^{-3/2})$ (C 4b) is significant, because it is smaller than the MF-contribution $-\mathfrak{U}(t) = O(t^{-1/2})$ to the entire radial velocity u (C 1a) by a factor $O(t^{-1})$. However, $\breve{u}^{\leftrightarrows}$ contributes to every term $\breve{u}_l$ in $\sum_{-\infty}^{\infty}\breve{u}_l$, and so its accumulated effect in the infinite sum might be far larger than that of $\breve{u}_0^{\leftrightarrows} = \breve{u}^{\leftrightarrows}$ alone. To assess this possibility, we take the z-average of u across the layer, noting the zero volume flux condition $0 = \langle u\rangle = -\mathfrak{U}(t) + \sum_{-\infty}^{\infty}\langle\breve{u}_l\rangle$. Then aided by the translational symmetry (C 1b) the integral of the sum may be expressed as a single integral and the result reorganised as

$$-\sum_{-\infty}^{\infty}\langle\breve{u}_l^{\leftrightarrows}\rangle = -\mathfrak{U}(t) + \sum_{-\infty}^{\infty}\langle\breve{u}_l^{\urcorner}\rangle = -\mathfrak{U}(t) + \tfrac{1}{2}\int_{-\infty}^{\infty}\breve{u}^{\urcorner}\,\mathrm{d}z\,. \qquad (\mathrm{C}\,6a)$$

Here the infinite integral of $\breve{u}^{\urcorner}$ may be recast using $x^{-1}\mathrm{d}z = -\mathsf{x}^{-2}|\mathsf{z}|^{-1}\mathrm{d}\mathsf{x}$ in the form of the principal value integral

$$\begin{aligned}
\tfrac{1}{2}\int_{-\infty}^{\infty}\breve{u}^{\urcorner}\,\mathrm{d}z &= \frac{1}{4\pi}⨍_{-1}^{1}\Big[\textstyle\sum_\pm\{\mathsf{x}_\pm^{-1/2}\}\sin(2\mathsf{x}t) + \sum_\pm\{\pm\mathsf{x}_\pm^{-1/2}\}\cos(2\mathsf{x}t)\Big]\dfrac{\mathrm{d}\mathsf{x}}{\mathsf{x}}\\
&= \frac{1}{2\pi}⨍_{-1}^{1}\left[\frac{1}{\mathsf{x}} + \frac{1}{\sqrt{\mathsf{x}_-}} - \frac{1}{1+\sqrt{\mathsf{x}_-}}\right]\big[\sin(2\mathsf{x}t) - \cos(2\mathsf{x}t)\big]\mathrm{d}\mathsf{x}\\
&= \frac{1}{\pi}\int_0^{2t}\frac{\sin\phi}{\phi}\,\mathrm{d}\phi\\
&\quad - \frac{\cos(2t)}{2\pi t}\int_0^{2t}\left[\frac{1}{\sqrt{\tau/t}} - \frac{1}{(1+\sqrt{\tau/t})}\right]\big[\sin(2\tau) + \cos(2\tau)\big]\,\mathrm{d}\tau\\
&\quad + \frac{\sin(2t)}{2\pi t}\int_0^{2t}\left[\frac{1}{\sqrt{\tau/t}} - \frac{1}{(1+\sqrt{\tau/t})}\right]\big[\cos(2\tau) - \sin(2\tau)\big]\,\mathrm{d}\tau\\
&= \frac{1}{2} - \frac{\cos(2t)}{\sqrt{4\pi t}} + \frac{1}{4\pi t}\sin(2t-\pi/4) + \cdots\cdots \qquad \text{for} \qquad t \gg 1\,. \qquad (\mathrm{C}\,6b)
\end{aligned}$$

Recalling that $\mathfrak{U}(t) = \frac{1}{2} - (4\pi t)^{-1/2}\cos(2t) + O(t^{-3/2})$ (see (1.15b) and (A 5)), the asymptotic result,

$$-\sum_{-\infty}^{\infty}\langle\breve{u}_l^{\leftrightarrows}\rangle = (4\pi t)^{-1}\sin(2t-\pi/4) + O(t^{-3/2}) \qquad \text{for} \qquad t \gg 1\,, \qquad (\mathrm{C}\,6c)$$

follows. Except for an amplitude change and phase shift, this has the same power law t^{-1} dependence on time, as the leading order $\mathfrak{C}$-trigger result $\langle u_{ms}\rangle = -\langle u_{bl}\rangle = -(2\pi t)^{-1}\cos(2t)$ given by the formulae ($\mathcal{O}$: 5.10), ($\mathcal{O}$: 5.11), where $\langle u_{bl}\rangle$ corresponds to our cut-contribution $\sum_{-\infty}^{\infty}\langle \breve{u}_l^{\leftrightarrows}\rangle$ (C 6*c*). The small size, $O(t^{-1})$, of (C 6*c*) is important because it shows that at $O(t^{-1/2})$ the dominant cut-contribution $-\mathfrak{U}_{MF}(t) \approx (4\pi t)^{-1/2}\cos(2t)$ is compensated by the accumulation of the inertial waves $\frac{1}{2}\int_{-\infty}^{\infty}\breve{u}^{\urcorner}\,\mathrm{d}z$ (C 6*b*). This largely explains the cancellation discussed in the penultimate paragraph of §3.2, where the result (C 6*c*) is alluded to.

C.2. *Individual z-Fourier m-modes*

Here we adapt the 'individual z-Fourier m-modes' analysis of §$\mathcal{O}$:6 to our problem. Quite simply, for $t \gg 1$ the dominant contributions $\widetilde{\chi}_m$ (see (2.6)) for given m, extracted from their LT by the method of steepest descent (equivalently, stationary phase) are two modulated waves

$$\widetilde{\chi}_{\pm}(x,t;\alpha_{\pm}) \propto \sin(\varPhi_{\pm}(x,t) \pm \pi/4 - \alpha_{\pm}) \tag{C 7a}$$

(cf. ($\mathcal{O}$: 6.16)) with phase

$$\varPhi_{\pm} = k_{\pm}x + \omega_{\pm}t\,, \qquad \text{where} \qquad k_{\pm} = 2m\pi\varphi_{\pm}/\omega_{\pm}\,. \tag{C 7b,c}$$

The two waves $\widetilde{\chi}_{\pm}$ stem from the saddle point crossings of the inverse-LT contour of integration at

$$p = \mathrm{i}\omega_{\pm}\,, \qquad 0 < \omega_+ < \omega_- < 2\,, \tag{C 8a}$$

where

$$\omega_{\pm} = 2\sqrt{1-\varphi_{\pm}^2}\,, \qquad 1 > \varphi_+ > \varphi_- > 0 \tag{C 8b}$$

(see ($\mathcal{O}$: 6.6*e*,*f*)). Here, the frequency $\omega_{\pm}$ and wavenumber $k_{\pm}$ (C 7*c*) are generated by $\varphi_{\pm}$, which are the two real positive roots of

$$\varphi^3 - \varphi + \vartheta^2 = 0 \qquad \text{with} \qquad \vartheta = \sqrt{m\pi x/(2t)} \tag{C 8c,d}$$

($\mathcal{O}$: 6.6*d*), ($\mathcal{O}$: 6.3*a*), which only exist when $\vartheta < \vartheta_c = 2^{1/2}\cdot 3^{-3/4}$ (C 11*b*).

To connect to the corresponding $\mathfrak{C}$-responses, we begin by expressing them ($\mathcal{O}$: 6.16) in the style of (C 7*a*) with the additional phase shift $-\alpha_{\pm}$. Thus, in terms of the extended function $\widetilde{\chi}^{\mathfrak{C}}_{\pm}(x,t;\alpha_{\pm})$, the actual value of ($\mathcal{O}$: 6.16) is $\widetilde{\chi}^{\mathfrak{C}}_{\pm}(x,t;0)$. By this device, our new $\mathfrak{W}$-responses, which generate $\widetilde{\chi}_m = \widetilde{\chi}_+ + \widetilde{\chi}_-$, may be written simply as

$$\widetilde{\chi}_{\pm}(x,t;\alpha_{\pm}) = \varphi_{\pm}^{-1}\,\widetilde{\chi}^{\mathfrak{C}}_{\pm}(x,t;\alpha_{\pm})\,, \tag{C 9a}$$

i.e., with an amplitude increase by $\varphi_{\pm}^{-1}$ and phase shifts $\alpha_{\pm}$ related, as in (2.13*a*), by

$$\alpha_{\pm} = \tfrac{1}{2}\cos^{-1}\varphi_{\pm}\,, \qquad 0 < \alpha_+ < \alpha_- < \pi/4\,. \tag{C 9b}$$

For $\vartheta \ll 1$, the two relevant positive roots of (C 8*c*) are approximately $\varphi_+ \approx 1 - \frac{1}{2}\vartheta^2$ and $\varphi_- \approx \vartheta^2$, which with (C 7) and (C 8) determine the phases

$$\varPhi_+ \approx \vartheta^{-1}m\pi x + 2\vartheta t = 4\vartheta t\,, \qquad \alpha_+ \approx \tfrac{1}{2}\vartheta\,, \tag{C 10a,b}$$

$$\varPhi_- \approx \vartheta^2 m\pi x + (2-\vartheta^4)t = (2+\vartheta^4)t\,, \qquad \alpha_- \approx \pi/4 - \vartheta^2/2 \tag{C 10c,d}$$

(use $m\pi x = 2\vartheta^2 t$ (C 8*d*)). For our purpose, it is sufficient to note the lowest order consequence

$$\widetilde{\chi}_+ \approx \frac{\sin(4\vartheta t + \pi/4)}{\sqrt{2\pi\vartheta t}}\,, \qquad \widetilde{\chi}_- \approx -\frac{\cos(2t)}{\sqrt{\pi t}}\,. \tag{C 10e,f}$$

The first low frequency ($\omega_+ \approx 2\vartheta$) term $\widetilde{\chi}_+$ is identical to the $\mathfrak{C}$-triggered mode $\widetilde{\chi}_+^{\mathfrak{C}}$ in ($\mathcal{O}$: 6.19), in which $X = 2\vartheta t$. However, relative to $\widetilde{\chi}_-^{\mathfrak{C}}$, the second MF-mode $\widetilde{\chi}_-$ is phase shifted by $\pi/4$ but more significantly magnified by the large factor $\varphi_-^{-1} \approx \vartheta^{-2}$. This increased size is interesting because $\widetilde{\chi}_-$ (C 10f) is simply the cut-contribution $\widetilde{\chi}_m^{\leftrightarrows}$ (see (3.9b) with $r/\ell \approx 1$). Nevertheless, despite its increased size, $\widetilde{\chi}_-$ remains smaller than $\widetilde{\chi}_+$, albeit by a less significant factor $O(\vartheta^{1/2})$, and is therefore formally negligible. As ϑ increases, the influence of the cuts on the 'stationary phase' solution $\widetilde{\chi}_-$ decreases too. We conclude that the cut-contribution (3.9b) that has caused concern is always negligible for $t \gg 1$.

On the one hand, the m-summation of $\widetilde{\chi}_+$, like $\widetilde{\chi}_+^{\mathfrak{C}}$ before, is justifiable in certain parameter ranges, and recovers the fan like behaviour mentioned in appendix C.1. On the other hand, the summation applied to $\widetilde{\chi}_-$, like $\widetilde{\chi}_-^{\mathfrak{C}}$ before, is invalid and meaningless, because as m increases the assumption that $\vartheta \ll 1$ is eventually violated. Thus there is no conflict with the conclusion of appendix C.1 that there are two MF-contributions to the entire triggered waves, one from the cuts and one from the poles, which when combined cancel. Rather our present restriction to a single m sheds no light on that matter.

On increasing ϑ, the $\omega_\pm$-saddle points approach each other. The corresponding roots $\varphi_\pm$ coalesce at $\varphi = \varphi_c$, where

$$\varphi_c = 3^{-1/2}, \qquad \vartheta_c = 2^{1/2} \cdot 3^{-3/4} \tag{C 11a,b}$$

($\mathcal{O}$: 6.20a,b) to produce a wave $\propto \sin(k_c x + \omega_c t - \alpha_c)$, for which ($\mathcal{O}$: 6.21) gives

$$(m\pi)^{-1} k_c = 2^{-1/2}, \qquad \omega_c = 2^{3/2} \cdot 3^{-1/2}, \qquad \alpha_c = \tfrac{1}{2}\cos^{-1}\varphi_c\,. \tag{C 11c–e}$$

Of course, this wave is modulated such that for $x > x_c = (m\pi)^{-1} 2\vartheta_c^2 t$ (see ($\mathcal{O}$: 6.21c), ($\mathcal{O}$: 6.22)) it is evanescent: $x = x_c$ is a fuzzy wave front. The spatial phase shift

$$\alpha_c/k_c \approx m^{-1} \times 0.215\,, \tag{C 12}$$

determined from (C 11c,e), is consistent with the node-shifts visible towards the left of panels (b), (d) of figures 1, 2, albeit for $E = 10^{-4}$. Again, near $x = x_c$, (C 11a) predicts a mode amplification of $\chi_{\mathfrak{W}}^{\sim}$ (panels (b)) by a factor $\varphi_c^{-1} = \sqrt{3}$ relative to $\chi_{\mathfrak{C}}^{\sim}$ (panels (d)), also evident. As noted by Oruba *et al.* (2020), such comparisons near the front lie well outside the domain of validity for our large ℓ asymptotics, which requires $\ell - r = x_c \ll \ell$. So any comparison with the figures is illustrative rather than quantitative.

REFERENCES

Abramowitz, M. & Stegun, I. A. 2010 *NIST Handbook of Mathematical Functions* (ed. F.W.J. Olver, D.W. Lozier, R.F. Boisvert and C.W. Clark). CUP. Available at: http://dlmf.nist.gov/.

Atkinson, J.W., Davidson, P.A. & Perry, J.E.G. 2019 Dynamics of a trapped vortex in rotating convection.

Benton, E.R. & Clark, A. 1974 Spin-up. *Annu. Rev. Fluid Mech.* **6**, 257–280.

Cederlöf, U. 1988 Free-surface effects on spin-up *J. Fluid Mech.* **187**, 395–407.

Chen, S., Lu, Y., Li, W. & Wen, Z. 2015 Identification and analysis of high-frequency oscillations in the eyewall of tropical cyclones. *Adv. Atmos. Sc.* **32**, 624–634.

Duck, P.W. & Foster, M.R. 2001 Spin-up of homogeneous and stratified fluids. *Annu. Rev. Fluid Mech.* **33**, 231–63.

Erdélyi, A., Magnus, W., Oberhettinger, F., Tricomi, F.G. *Tables of Integral Transforms (Director A. Bateman)*, vol. I. McGraw-Hill Book Company.

Fischer, M.S., Rogers, R.F. & Reasor, P.D. The rapid intensification and eyewall replacement cycles of hurricane Irma (2017). *Mon. Wea. Rev.* **148**, 981–1004.

Greenspan, H.P. 1968 *The Theory of Rotating Fluids*. Cambridge University Press.

Greenspan, H.P. & Howard, L.N. 1963 On a time-dependent motion of a rotating fluid. *J. Fluid Mech.* **17**, 385–404.

Harlow, F.H. & Stein, L.R. 1974 Structural analysis of tornado-like vortices. *J. Atmos. Sci.* **31**, 2081–2098.

Houze Jr., R.A., Chen, S.S., Smull, B.F., Lee, W.-C. & Bell, M.M. Hurricane intensity and eyewall replacement. *Science* **315**(5816), 1235–1239.

Kerswell, R.R. & Barenghi, C.F. 1995 On the viscous decay rates of inertial waves in a rotating circular cylinder. *J. Fluid Mech.* **285**, 203–214.

Klein, M., Seelig, T., Kurgansky, M.V., Ghasemi V., A., Borcia, I.D., Will, A., Schaller, E., Egbers, C. & Harlander, U. 2014 Inertial wave excitation and focusing in a liquid bounded by a frustum and a cylinder. *J. Fluid Mech.* **751**, 255–297.

Kurgansky, M.V., Seelig, T., Klein, M., Will, A. Harlander 2020 Mean flow generation due to longitudinal librations of sidewalls of a rotating annulus. *Geophys. Astrophys. Fluid Dynam.* online: 20 Jan. 2020, doi.org/10.1080/03091929.2019.1692829.

Montgomery, M.T., Snell, H.D. & Yang, Z. 2001 Axisymmetric spindown dynamics of hurricane-like vortices. *J. Atmos. Sci.* **58**, 421–435.

Oruba, L., Soward, A.M. & Dormy, E. 2017 Spin-down in a rapidly rotating cylinder container with mixed rigid and stress-free boundary conditions. *J. Fluid Mech.* **818**, 205–240.

Oruba, L., Soward, A.M. & Dormy, E. 2020 On the inertial wave activity during spin-down in a rapidly rotating penny shaped cylinder: a reduced model. *J. Fluid Mech.* **888**, A9, 1–44.

Read, P.L. 1986*a* Super-rotation and diffusion of axial angular momentum. I. "Speed limits" for axisymmetric flow in a rotating cylindrical fluid annulus. *Q. J. R. Meteorol. Soc.* **112**, 231–251.

Read, P.L. 1986*b* Super-rotation and diffusion of axial angular momentum. II. A review of quasiaxisymmetric models of planetary atmospheres. *Q. J. R. Meteorol. Soc.* **112**, 253–272.

Rotunno R. 1979 A study in tornado-like vortex dynamics. *J. Atmos. Sci.* **36**, 140–155.

Rotunno, R. 2014 Secondary circulations in rotating-flow boundary layers. *Aust. Meteor. Ocean.* **64**, 27–35.

Rotunno, R. & Emanuel, K.A. 1987 An airsea interaction theory for tropical cyclones. Part II: Evolutionary study using a nonhydrostatic axisymmetric numerical model. *J. Atmos. Sci.* **44**, 542–561.

Williams, G.P. 1968 Thermal convection in a rotating fluid annulus: part 3. Suppression of the frictional constraint on lateral boundaries. *J. Atmos. Sci.* **25**, 1034–1045.

Yarom, E. & Sharon, E. 2014 Experimental observation of steady inertial wave turbulence in deep rotating flows. *Nature Phys.* **10**, 510–514.

Zhang, K. & Liao, X. 2008 On the initial-value problem in a rotating circular cylinder. *J. Fluid Mech.* **610**, 425–443.

Zhang, K. & Liao, X. 2017 *Theory and Modeling of Rotating Fluids: Convection, Inertial Waves and Precession.* Cambridge University Press.